International Journal of Material Science (IJMSCI) Volume 4 Issue 1, March 2014 www.ij-ms.org
doi: 10.14355/ijmsci.2014.0401.01

Effect of a Surfactant Assisted Synthesis on the Electrochemical Performance of a $LiFePO_4$-CNT Composite Electrode

Ulla Lassi[*1,4], Tao Hu[2], Elina Pohjalainen[3], Tanja Kallio[3], Krisztian Kordas[2], Heli Jantunen[2]

[1] University of Oulu, Department of Chemistry, FIN-90014 Oulu, Finland
[2]University of Oulu, Microelectronics and Materials Physics Laboratories, FIN-90014 Oulu, Finland
[3]Aalto University School of Chemical Technology, Department of Chemistry, P.O. Box 16100, FI-00076 Aalto, Finland
[4]Kokkola University Consortium Chydenius, Department of Applied Chemistry, FIN-67701 Kokkola, Finland
[*1]ulla.lassi@oulu.fi; [2]tao.hu@oulu.fi; elina.pohjalainen@aalto.fi

Abstract

This research aims at improving the performance of lithium iron phosphate ($LiFePO_4$) positive electrode material by using carbon nanotubes (CNT) to increase the conductivity and nonionic surfactant to achieve better dispersion of CNTs in the composite material. $LiFePO_4$-CNT composites were synthesized by the wet chemical method and functionalized multi-walled carbon nanotubes MWCNT-COOH were added in-situ. The nonionic surfactant polyoxyethylene-oleyl ether (E-230) was used to enhance the dispersion of MWCNT in the $LiFePO_4$nanopowder and removed during the last step of the synthesis to avoid possible unwanted side reactions of the surfactants in the battery. During this last step, the composite materials were heated at 500-700°C in an Ar-H_2 atmosphere for several hours. XRD, DTA/TG, FESEM and EFTEM were used for characterization of the crystallization and microstructure of the obtained composites. Electrochemical performance was characterized by charging and discharging experiments with various C-rates using standard lithium ion battery half cells. Results showed that the addition of MWCNT-COOH and the surfactant E-230 remarkably increased the obtained capacities of $LiFePO_4$. Acting as a dispersant and interfacial coupling agent, the nonionic surfactant enhanced the dispersion of carboxylic MWCNT into the $LiFePO_4$ during the in-situ synthesis and enhanced the specific capacity of the tested composites.

Keywords

Lithium-ion Battery; Lithium Iron Phosphate; Carbon Nanotube; $LiFePO_4$-MWCNT Composite; In-situ Synthesis; Charge/ Discharge; Electrochemical Performance

Introduction

Lithium ion batteries have become the most popular rechargeable batteries since their market introduction some 20 years ago because of their high energy and power density, and good cycle ability. Intensive research on electrodes, electrolytes and battery systems has been carried out all over the world to improve the performance and safety, and to reduce the price of the devices to facilitate market penetration of lithium ion batteries as a power source in hybrid electric vehicles and electric vehicles [Armand &Tarascon, 2008; Patil et al., 2008; Wang &Cao, 2008; Park et al., 2010; Stephan & Nahm, 2006; Zhao, Wang & Zhang, 2011; Ellis, Lee, &Nazar, 2010]. $LiFePO_4$ (LFP) is considered as one of the most promising cathode material with long cycle life and excellent safety [Yuan et al., 2011; Wang, He & Zhou, 2011; Muraliganth, Murugan & Manthiram, 2008]. However theoretical energy density of LFP has been difficult to achieve because of its low conductivity. Conductive carbon coatings on the particles have been shown to be a very effective way to enhance the conductivity of the electrode material. [Yuan et al., 2011] In recent years, multi-walled carbon nanotubes (MWCNTs) with high thermal and electrical conductivity, good mechanical strength, and high chemical stability have been widely used in different applications to achieve novel composite structures with advanced properties. MWCNT has been added in $LiFePO_4$ electrodes in Li-ion batteries as a conductive additive to enhance the electrical and thermal transport behaviour and to reduce battery polarization[Kang, Ma, &Li, 2011; Feng, 2010; Xu, Chen & Li, 2009; Zhou et al., 2010; Sun et al., 2012; Jin et al., 2008; Wu et al., 2011; Pei et al., 2012]. Composites of $LiFePO_4$ and MWCNTs can be prepared simply by dispersing the powders in solvents such as ethanol or N-methylpyrrolidone followed by drying [Feng, 2010; Xu, Chen & Li, 2009]. An addition of 5-7 wt.% of MWCNTs in the cathode material results in an increased initial discharge capacity of ~150-160 mAh/g

at a discharge rate of 0.18-0.30C with a capacity retention ratio of about 98% after 50-100 cycles, respectively. Similar results have been reported by other research groups with chemical vapour deposition, hydrothermal and other synthesis methods. [Zhou et al., 2010; Sun et al., 2012; Jin et al., 2008; Wu et al., 2011; Pei et al., 2012]

In this research paper, we report on an in-situ synthesis of $LiFePO_4$-MWCNT composite electrode materials aiming to achieve homogenious microstructures and better battery behavior. This in-situ wet chemical method is low cost, easy-controlled and less complex compared with other synthesis methods [Zheng et al., 2008], which synthesized amorphous $LiFePO_4$ using oxalic acid as a reducing agent at room temperature followed by calcination to form nanocrystalline $LiFePO_4$. In our experiments, the $LiFePO_4$-MWCNT nanocomposites are prepared using carboxyl functionalized multi-walled carbon nanotubes MWCNT-COOH (MC) which are added into the solution of starting reactants at the beginning of the synthesis. In order to obtain uniform CNT distribution in the composites a nonionic surfactant E-230 (polyoxyethylene-oleyl ether) was applied. The structural properties along with the charge and discharge behaviour of the composites are discussed.

Experimental

$LiFePO_4$ is synthesized by dissolving stoichiometric amounts of $FePO_4{\cdot}4H_2O$ (Alfa Aesar), $H_2C_2O_4$ (99.999%, Aldrich) and Li_2CO_3 (>99.0%, Aldrich) in water according to the chemical reaction

$$2FePO_4{\cdot}4H_2O + H_2C_2O_4 + Li_2CO_3 \rightarrow 2LiFePO_4 + 3CO_2 + 9H_2O$$

In a typical synthesis, 0.445 g $FePO_4{\cdot}4H_2O$ and 0.540 g $H_2C_2O_4$ were dissolved in 30 mL water during continuous stirring and heating below 100°C, followed by the addition of 0.745 g Li_2CO_3. A clear yellowish green solution was obtained. Multi-walled carbon nanotubes (>90%, Aldrich) were acid-treated to remove amorphouscarbon and metal catalyst residuals of synthesis. In a typical process, a 5 g sample was sonicated for 1 h and then refluxed for 8 h in 250 ml 70% HNO_3 followed by washing with deionized water and drying. 0.0186 g functionalized multi-walled carbon nanotubes MWCNT-COOH with or without surfactant E-230 were suspended in 30 ml water and sonicated for 1 h, then added in the previous yellowish green solution and sonicated for another hour. The precursor was then dried at 100°C, and heated at 550-700°C for 4-7 hours in a 15% H_2–Ar atmosphere. Black nanopowders of LFP-MC composites were obtained.

A nonionic surfactant NONION®E-230 (E-230, $C_{18}H_{35}O$-$(C_2H_4O)_n$-H with a hydrophile-lipophile balance of 16.6.) was provided by NOF Corporation (Japan). The LFP-MC sample E0 was a $LiFePO_4$-MWCNT composite with 5.4 wt% MWCNT-COOH synthetized without any surfactant whereas the LFP-MC samples E1-E5 were composites with 5.4 wt% MWCNT-COOH and synthesized with different weight percentage of surfactant E-230 (Table 1).

TABLE 1 THEDESIGNED COMPOSITIONS OF THELFP-MWCNT COMPOSITE SYNTHESIS

Sample No	E0	E1	E2	E3	E4	E5
$LiFePO_4$ (g)	0.315	0.315	0.315	0.315	0.315	0.315
MC (g)	0.018	0.018	0.018	0.018	0.018	0.018
E-230 (g)	0	0.025	0.050	0.108	0.165	0.253
E-230 (wt%)	0	7.0	13.1	24.5	33.1	43.2

The crystalline phases and structures were analysed by X-ray diffraction (Siemens D5000 XRD) whilst the morphology and microstructure were characterized by a transmission and field emission scanning electron microscopy (LEO 912 OMEGA EFTEM, Zeiss ULTRA plus FESEM, respectively). The thermal properties were analysed by TG/DTA thermogravimetry (NETZSCH STA 409 PC/PG).

Testing of the composite materials was conducted with standard coin cells (2032). Positive electrodes were prepared by mixing 80 wt% of active composite material, 15 wt% of Super P Li conductive carbon (Timcal), and 5 wt% of polytetrafluoroethylene binder (PTFE, Dupont) in *N*-methyl-pyrrolidone (NMP, Sigma-Aldrich). The mixture was rolled into a thin sheet and circular electrodes of 8 mm in diameter were cut out. A lithium metal foil (12 mm in diameter and 0.38 mm in thickness, Aldrich) was used as a counter electrode, a 25 μm thickness porous polymer membrane (Celgard 2300) as a separator and1M $LiPF_6$ in 1:1 ethylene carbonate: dimethyl carbonate (LP 30®, Merck) as an electrolyte in the coin cells. The coin cells were assembled in an argon filled glove box and at least three cells were assembled and measured for each sample. The charge/discharge properties were measured by a battery testing cycler (Neware multi-channel battery testing system) and galvanostatic charging and discharging was conducted within the voltage range of 2.5 – 4.1 V *vs*. Li/Li^+ at C-rates of 0.2C, 0.5C, and 1C with 10 cycles at each rate. C-rates were calculated using the theoretical capacity of 170 mAh/g of lithium iron phosphate, where 1C corresponds to charging/discharging in 1 h.

Results and Discussion

Comparison of LFP-MC Composites E0 and E5

The synthesized LFP-MC composites E0 were heated at temperatures of 550, 600, 650, 700, 750°C for 6 hours in a 15% H_2–Ar atmosphere and analyzed by XRD. The XRD pattern of each sample showed orthorhombic $LiFePO_4$ (PCPDF file of 01-070-6684). Higher annealing temperatures result in higher X-ray reflection intensities, i.e. better crystallization of the electrode material (Fig. 1). Based on the XRD results, the optimal heating temperature and time was identified as 650°C for 6 hours.

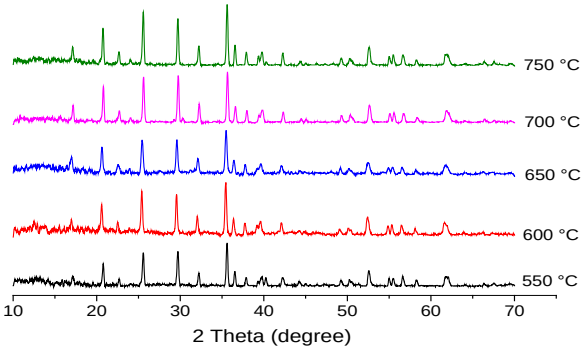

FIG. 1 XRD PATTERNS OF SAMPLE E0 HEATED AT DIFFERENT TEMPERATURES

Due to the agglomeration of the CNTs during the in-situ synthesis, the surfactant was added to enhance the dispersing of the nanotubes in LFP. Earlier, the nonionic surfactant Triton X-100 was reported to treat a CNT surface for nanocomposite fabrication [Geng et al., 2008]. The Triton X-100 serves as a bridge between CNTs and the epoxy matrix without disturbing the CNT structure or introducing defects. Mechanical, fracture and thermo-mechanical properties of the CNT-Epoxy composite all showed significant improvement after the surfactant treatment of CNT. In our experiments, the nonionic surfactant E-230 (polyoxyethylene-oleyl ether) is chosen.

The sample E5 with surfactant E-230 heated at 650°C for 6 hours showed similar XRD patterns to sample E0 without E-230 (Fig. 2). Scattering from MWCNTs cannot be identified due to the low content of MWCNT and also to the overlapping of reflections from the two phases, e.g. C(002) with $LiFePO_4$(111). The calculated crystallite size of $LiFePO_4$ heated at 650°C was 42.3± 2.3 nm for E5 from the (311) peak.

EFTEM image of LFP-MC composite E5 heated at 650°C for 6 hours is shown in Figure 3 which reveals LFP particle size in the range of 20-140 nm. The particles are mainly sphere shape.

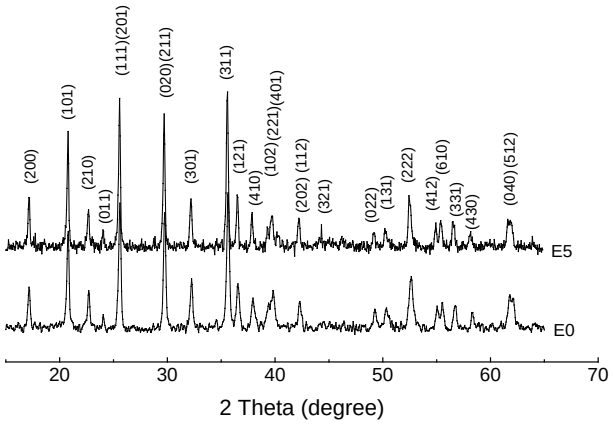

FIG. 2 XRD PATTERNSFOR THE SAMPLES E0 AND E5 HEATED AT 650 °C

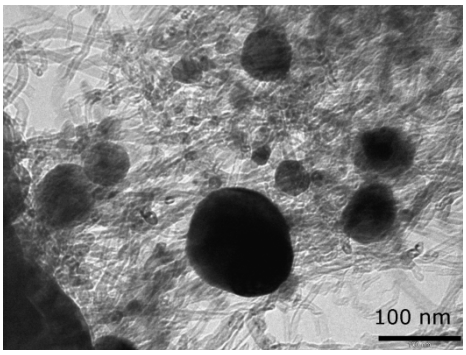

FIG. 3 EFTEM IMAGE OFSAMPLE E5

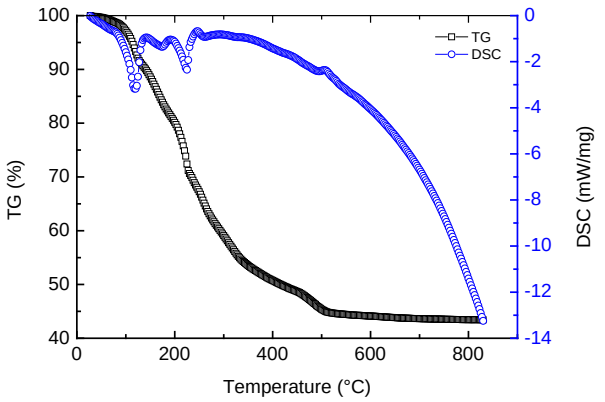

FIG. 4 THE TG/DSC CURVE OF SAMPLE E5

The TG-DSC analysis was performed in Helium atmosphere with a flow rate of 60 ml/min from 20 to 850°C with a heating rate of 20 °C/min. Weight loss of the samples started close to 100°C due to water evaporation with an endothermic peak at 120°C, which then continued with the decomposition of excess $H_2C_2O_4$ and the surfactant E-230 at around 200°C with an endothermic peak at 175 and 225°C (Figure 4). The exothermal peak appearing at 520°C denotes the crystallization of $LiFePO_4$ which also confirms that the chosen annealing temperature of 650°C in the synthesis is sufficient for the

crystallization of $LiFePO_4$. From Figure 4, the mass at 150°C was 88.6 wt%, which indicated that mass loss through the removal of water was 11.4 wt%. The total mass of the precursor was 43.4 wt% at 850°C, showing that a mass loss of 45.2 wt% was caused by the decomposition of surfactant E-230 and excess $H_2C_2O_4$. This loss fits well with the calculated E-230 content of 43.2 wt% in Table 1 and it can be therefore assumed that the surfactant was burned away completely after heating at 650°C.

FESEM images of E0 and E5 heated at 650°C for 6 hours are shown in Figure 5a and Figure 5b respectively. Comparison of these images reveals that the crystal morphologies of these samples differ. The sample E0 synthetized without surfactant E-230 showed a particle size of 0.1-2 μm with a well-crystallized rectangular shape whereas particle sizes of sample E5 are clearly smaller, 0.02-0.6 μm, and mainly spherical. It is obvious that surfactant E-230 limits the grain growth and affects the particle size and shape. The MC nanotubes are more homogeneously distributed in the sample E5 and show fewer bundles in the images.

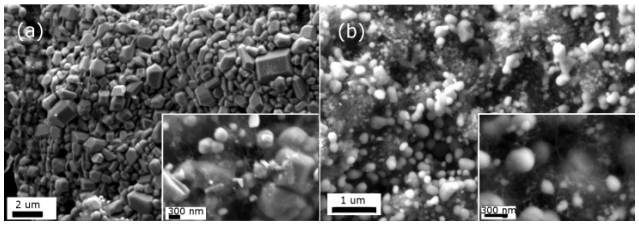

FIG. 5 FESEM IMAGES OF (a) E0 AND (b) E5 AFTER HEATING AT 650 °C FOR 6 HOURS

The electrochemical performance of the synthesized composites in lithium ion batteries was tested using standard half cells. The charge/discharge results of LFP-MC sample E0 were measured at a rate of 0.2C for 100 cycles (Fig. 6). The specific capacity for the 2nd cycle is 89 mAh/g. The charge and discharge curves show a flat plateau with rather small differences between the charging and discharging voltages. However, the capacities are well behind the theoretical values. This is partly due to the thickness of the composite electrodes as the loadings are 12-14 mg/cm^2 (active material loading 9-11 mg/cm^2) resulting in an electrode thickness of approximately 100 μm. Somewhat lower capacities are to be expected for electrodes with this high loading at higher C-rates [Fongy et al., 2010].

Charge/discharge profiles of the sample E5 are measured at a rate of 0.2C, 0.5C, 1C and 0.2C with 10 cycles each. The specific capacity of the E5 sample at rate of 0.2C for the 2nd cycle is 115 mAh/g, which is 26 mAh/g higher than for LFP-MC E0 at the same stage (Fig. 6). An increase in the capacity of LFP-MWCNT composite synthesized with the addition of surfactant E-230 is a combination of a more homogeneous distribution of MWCNTs and a reduction in the particle size of LFP (Fig. 5) that affects both the electronic and ionic conductivity of the composite electrode [Gaberscek, Dominko, Jamnik 2007].

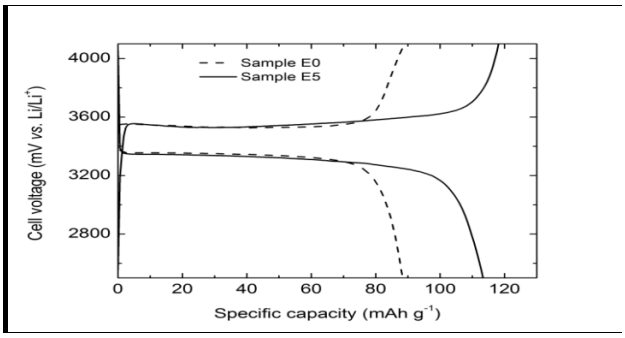

FIG. 6 CHARGE/DISCHARGECURVESOFSAMPLE E0 and E5AT 0.2CRATE

The specific capacity as a function of cycling for sample E0 and E5 are shown in Fig. 7. After 100 cycles the specific capacity of sample E0 at rate of 0.2C decreased to 82 mAh/g (7.5% reduction). For sample E5, the specific capacities decrease as increase of C-rates from 0.2C to 0.5C and 1C. However, the specific capacities are quite stable for certain C-rate. The specific capacities at 0.2C remain same values after several cycling with different C-rates.

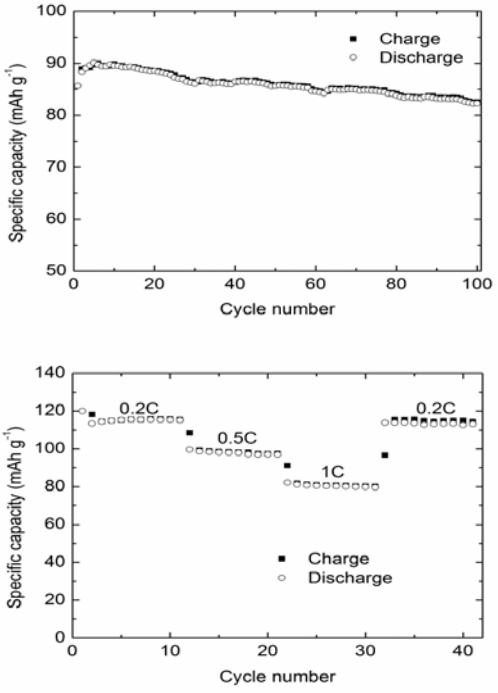

FIG. 7 SPECIFIC CAPACITY AS A FUNCTION OF CYCLING FOR SAMPLEE0AT 0.2C RATE ANDSPECIFIC CAPACITIES FOR E5AT DIFFERENT C-RATES

Effect of E-230 Concentration on LFP-MC Composites

Four other composites E1-E4 (Table 1) have been prepared in order to investigate the effects of the concentration of E-230 on the properties of the $LiFePO_4$. FESEM images of the four additional composite samples E1-E4 (Fig. 8) showed similar microstructures to composite E5 (Fig. 5b). The particle sizes of the composites were getting smaller when the amount of surfactant in the composites increased. EFTEM images of composites E1-E4 are shown in Fig. 9 which presents the microstructures of the composites. It has been confirmed that fewer particles with size up to 500 nm were observed in the composites prepared with higher surfactant concentration.

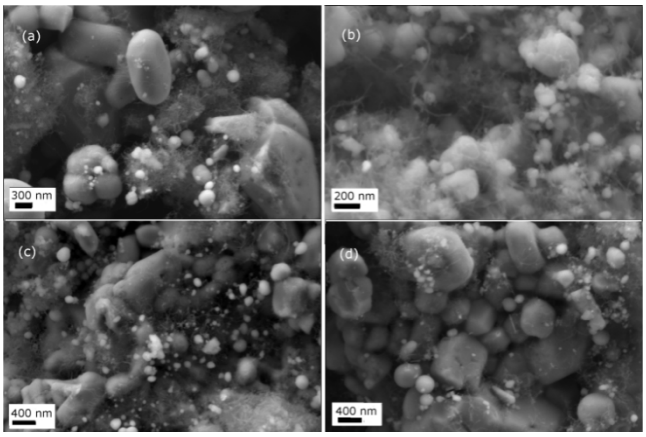

FIG. 8 FESEM IMAGES OF COMPOSITE SAMPLES (A) E1, (B) E2, (C) E3, AND (D) E4

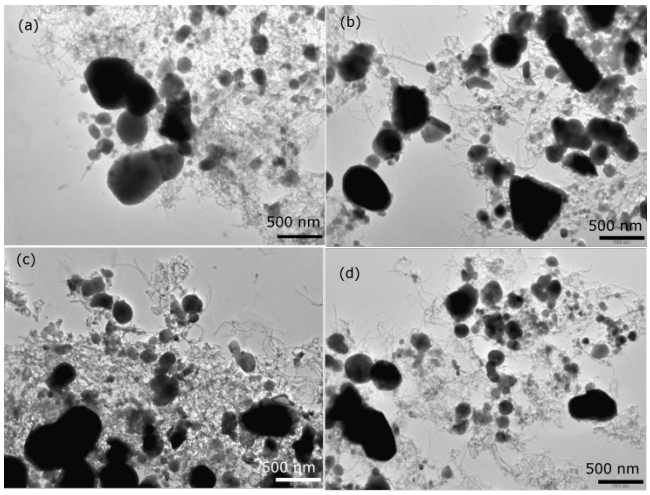

FIG. 9 EFTEM IMAGES OF COMPOSITE SAMPLES (A) E1, (B) E2, (C) E3, AND (D) E4

Coin cells have been prepared for each sample (E1-E4) and their charge/discharge properties were measured in the same way as for E0 and E5. Charge/discharge tests of E1-E4 have been measured at rates of 0.2C, 0.5C, 1C, and 0.2C with 10 cycles each. The obtained charge and discharge curves for E1-E4 are similar to E5 (Fig. 8). The average specific capacity values (mAh/g) for ten cycles at 0.2C are listed in Table 2 in which the calculated error of the specific capacity based on the measurement accuracy of electrode mass is approximately ±2 mAh/g. Samples E1, E2, and E3 with the lowest amounts of surfactant, 7.0% 13.1% and 24.5% respectively, achieved similar discharge capacities of 91-95 mAh/g, which can be considered equal within the experimental error. Samples E4 and E5 with higher amounts of surfactant, 33.1% and 43.2% respectively, showed higher discharge capacities, 106 mAh/g (E4) and 115 mAh/g (E5). Thus it can be concluded that surfactant E-230 when used in the synthesis improves the specific capacities of the obtained LFP-MWCNT composites, and the increase in capacity is higher with higher surfactant amounts.

TABLE 2 AVERAGE SPECIFIC CAPACITY VALUES (MAH/G) FOR TEN CYCLES AT 0.2C

	E1	**E2**	**E3**	**E4**	**E5**
Charging	96	91	93	107	115
Discharging	95	91	92	106	115

Conclusions

Positive electrode materials based on $LiFePO_4$ and MWCNTs were researched to improve the power density of a Li-ion battery. During the synthesis of LFP-MWCNT composites, the nonionic surfactant E-230 was added in-situ to enhance the distribution of carboxylic MWCNT in the LFP composite. Five composite samples were prepared with different amounts of E-230 to study the effects of E-230 on the electrochemical performance of the LFP electrode, and to find out the optimum content of the non-ionic surfactant in the synthesis. The nonionic surfactant serving as a dispersant and an interfacial coupling agent, increased the dispersion of carboxylic MWCNT and inhibited the particle growth during the in-situ synthesis of the LFP composite electrode material. Therefore, more homogenious structures were obtained and the electrochemical performance of the composite electrodes in lithium ion battery half cells was enhanced.

ACKNOWLEDGMENT

The authors would like to acknowledge the "Teknologiateollisuus 100v foundation" from the Federation of Finnish Technology Industries (Project NANOLI), Tekes project IMPOLI, and the Fortum Foundation of Finland (No 11-153) for their financial support of this research.

REFERENCES

Armand, M.,and Tarascon, J.-M."Building better batteries." Nature 451 (2008): 652-657.

Cao, A., Xu, C., Liang, J., Wu, D., Wei, B. "X-ray diffraction characterization on the alignment degree of carbon nanotubes." Chem. Phys. Lett. 344 (2001): 13-17.

Ellis, B.L., Lee, K.T., and Nazar, L.F."Positive electrode Materials for Li-ion and Li-Battery." Chem. Mater. 22 (2010): 691–714.

Feng,Y. "The preparation and electrochemical performances of $LiFePO_4$-multiwalled nanotubes composite cathode materials for lithium ion batteries."Mater. Chem. Phys. 121 (2010): 302-307.

Fongy,C., Gaillot,A.-C., Jouanneau,S., Guyomard,D., Lestriez, B. "Ionic vs Electronic Power Limitations and Analysis of the Fraction of Wired Grains in $LiFePO_4$ Composite Electrodes," J. Electrochem. Soc., 157 (7) (2010): A885-A891.

Gaberscek,M., Dominko,R., Jamnik,J. "Is small particle size more important than carbon coating? An example study on $LiFePO_4$ cathodes." Electrochemistry Communications 9 (2007): 2778–2783.

Geng,Y., Liu,M.Y., Li,J., Shi,X.M., Kim, J.K. "Effects of surfactant treatment on mechanical and electrical properties of CNT/epoxy nanocomposites." Composites: Part A 39 (2008): 1876–1883.Stephan, A.M., Nahm, K.S."Review on composite polymer electrolytes for lithium batteries." Polymer 47 (2006): 5952-5964.

JinB., Jin,E.M., Park, K.-H.,Gu, H.-B. "Electrochemical properties of $LiFePO_4$-multiwalled carbonnanotubes composite cathode materials for lithium polymer battery." Electrochemistry Communications 10 (2008): 1537–1540.

Kang,F., Ma,J., Li,B. "Effects of carbonaceous materials on the physical and electrochemical performance of a $LiFePO_4$ cathode for lithium-ion batteries." New Carbon Materials 26 (2011): 161–170.

Muraliganth,T., Murugan,A.V., and Manthiram, A."Nanoscale networking of $LiFePO_4$nanorods synthesized by a microwave solvothermal route with carbon nanotubes for lithium ion batteries." J. Mater. Chem. 18 (2008): 5661–5668.

Park, C.-M., Kim, J.-H., Kim, H., and Sohn H.-J."Li-alloy based anode materials for Li secondary batteries." Chem. Soc. Rev., , 39 (2010): 3115–3141.

Patil, A., Patil, V., Shin, D.W., Choi, J.-W., Paik, D.-S., Yoon, S.-J. "Issue Challenge facing rechargeable thin film Li battery." Materials Research Bulletin 43 (2008): 1913–1942.

Pei,B., Yao,H., Zhang,W., Yang, Z. "Hydrothermal synthesis of morphology-controlled $LiFePO_4$ cathode material for lithium-ion batteries." Journal of Power Sources 220 (2012): 317–323.

Sun,X., Li,J., Shi, C., Wang,Z., Liu,E., He,C., Du,X., Zhao, N."Enhanced electrochemical performance of $LiFePO_4$ cathode with in-situ chemical vapor deposition synthesized carbon nanotubes as conductor." Journal of Power Sources 220 (2012): 264–268.

Wang, Y.and Cao, G."Developments in Nanostructured Cathode Materials for High-Performance Lithium-Ion Batteries." Adv. Mater. 20 (2008): 2251–2269.

Wang,Y., He, P., and Zhou, H. "Olivine $LiFePO_4$: development and future." Energy Environ. Sci. 4 (2011): 805–817.

Wu,C.Y., Cao, G.S.,Yu, H.M.,Xie, J., Zhao, X.B. "In Situ Synthesis of $LiFePO_4$/Carbon Fiber Composite by Chemical Vapor Deposition with Improved Electrochemical Performance." J. Phys. Chem. C 115 (2011): 23090-23095.

Xu,J., Chen,G., Li, X. "Electrochemical performance of $LiFePO_4$ cathode material coated with multi-wall carbon nanotubes." Mater. Chem. Phys. 118 (2009): 9-11.

Yuan,L., Wang, Z., Zhang, W., Hu, X., Chen,J., Huang,Y., and Goodenough, J.B. "Development and challenges of $LiFePO_4$ cathode materials for Li-ion battery." Energy Environ. Sci. 4 (2011): 269-284.

Zhao, D., Wang, Y., Zhang, Y."High-Performance Li-ion Batteries and Supercapacitors based on Prospective 1-D Nanomaterials."Nano-Micro Lett. 3 [1] (2011): 62-71.

Zheng, J., Li, X., Wang, Z., Guo, H., Zhou, S. "$LiFePO_4$ with enhanced performance synthesized by a novel synthetic route." J. Power Sources 184 (2008) 574-577.

Zhou,Y., Wang, J., Hu, Y., O'Hayre,R., Shao, Z. "A Porous $LiFePO_4$ and Carbon Nanotube Composite." Chem. Commun. 46 (2010): 7151-7153.

Ulla M. Lassi is the head of research unit of Applied Chemistry at the University of Oulu, Finland. She received her PhD in chemical engineering at the University of Oulu in 2003, and M.Sc. (Chem.) in 1996 and M.Sc. (Chem. Eng.) in 1998 at the same university. She was appointed as a full

professor in Applied Chemistry and Process Chemistry in 2006. Her main research areas involve catalytic materials in process and environmental applications as well as Li ion battery chemicals.

Tanja Kallio is heading a group specialized in electrochemical energy conversion applications at Aalto University Department of Chemistry, Finland. She has completed M.Sc. (Tech.) and D.Sc. (Tech.) in chemical engineering in the year 1998 and 2003, respectively, at Helsinki University of Technology, Finland. Her research interests include electrocatalysis of direct alcohol fuel cells and electrochemistry of electroactive materials for lithium ion batteries and super capacitors. Dr. Kallio has some 40 publications in peer-reviewed journals.

doi: 10.14355/ijmsci.2014.0401.02

The Fabrication and Calibration of an Iridium pH Micro-sensor for Biological Applications

Francesco Contu*, Manuel Vega-Arroyo, S. Ray Taylor

The National Corrosion Center, Texas A&M Engineering Experiment Station
6815 Rustic St. Houston, TX 77087

francescocontu@tees.tamus.edu

Abstract

A metal-metal oxide electrode based on the pH sensitivity of the redox equilibrium reactions between Ir(IV) and Ir(III) oxides was prepared for biological applications. Electrodes were prepared using multiple voltage sweeps, coated with a proton conducting membrane, followed by a water soak. It was shown that prior to testing the pH of biological media, it was necessary to calibrate the sensor in proteinaceous solutions. Results obtained from calibration experiments conducted in inorganic buffers, fetal bovine serum and artificial saliva show a sensitivity of 47 mV/pH and time response of 50 seconds.

Keywords

Iridium; Sensor; pH; Calibration; Cell Culture Media; Serum

Introduction

PH monitoring is critical for human health since a constant pH level is essential for biological and biochemical processes. For example, in the case oral health, a critical pH of 5.5 has been identified below which the development of dental caries is kinetically accelerated. It is known that oral biofilms have the potential to decrease the pH below this threshold level. This and other examples have boosted the development of pH sensors for biological applications. One challenge that remains in the development of pH micro-sensors is the ability to quantitatively assess the pH within the micro-gaps that develop between teeth and dental restoration materials, and within acidogenic and aciduric bacterial colonies. Among commercially available pH microsensors, the glass pH electrode has been widely used for biological applications. However, its slow response and mechanical and difficult miniaturization have led to the development of more versatile pH microsensors.

One of the most reliable pH microsensors is based on metal-oxide electrodes. Such sensors rely on the pH sensitivity of redox reaction between a metal and its oxide (e.g. Sb/Sb_2O_3) or between two oxides (e.g. Ir(III)/Ir(IV) oxides). Metal-metal oxide electrodes that can be easily miniaturized, having very good pH response, are mechanically stable and relatively free from cation interferences. Several pH sensors are based on metal oxides include PtO_2, TiO_2, IrO_x, RuO_2 , RhO_2, Ta_2O_5 and SnO_2. Among these metal oxides, IrO_x (iridium oxides) has been considered one of the best for pH-sensing. Iridium oxide has the advantage of having potential stability over a wide range of temperature and pressure, Nernstian sensitivity in the range of 55 to 77 mV/pH, low sensitivity to redox interferences, has the ability to be easily miniaturized. Some of the techniques used to fabricate pH-sensors based on iridium oxide include: (a) deposition techniques such as sputtering and electrodeposited iridium oxide films (EIROF), (b) sol-gel processes, and (c) anodized iridium oxide films (AIROF).

The goal of this research was to prepare an electrochemically oxidized iridium microelectrode (AIROF) and document its sensitivity and response time to measure the local pH in oral biofilms. The oxidized wire was dip-coated with a Nafion® film to assure proton conductivity while preventing proteins from reaching the iridium oxides and disrupting its response. The work presented here is the first step of a multidisciplinary effort aimed to incorporate iridium micro-sensors within artificial micro-gaps exposed to oral biofilms to monitor the pH within the resulting occluded chemistry.

Materials and Method

Chemicals and Materials

Experiments were conducted using an iridium (Ir) wire (E-filaments LLC, 99.91%) with a diameter of 0.5 mm and exposed surface area of 0.159 cm^2 unless otherwise stated. Reagent grade chemicals and 18 MOhm distilled water were used. Fetal bovine serum was purchased from Sigma-Aldrich and cell culture media Casamino Medium Mucin (CAMM) where the following bacteria were grown: Fusobacterium

nucleatum, Streptococcus mutans, Veillonella dispar and Actinomyces odontolyticus. The bacteria were cultured on CDC Anaerobe 5% Sheep Blood agar. *V. dispar* was cultured in medium supplemented with 1.5% sodium lactate. Incubation was at 37°C in an anaerobic chamber (Coy Laboratory Products) in the presence of 85% N_2, 10% CO_2, and 5% O_2.

Electrode Preparation

The Ir wire was mechanically wet-polished to 4000 SiC paper and thereafter ultrasonically cleaned in distilled water for 10 minutes. Then it was immersed in 0.5M sulfuric acid and electrochemically oxidized using a using a Solarton™ 1286 Electrochemical Interface that applied a triangular potential sweep between 0.0 and 1.25 V vs. a saturated calomel electrode (SCE) at a potential scan rate of 100 mV/s for up to 650 cycles. The oxidized electrode was subsequently rinsed with distilled water and coated by dipping in a 5% or 2.5% Nafion® solution (75% isopropanol in water) for 1 hour and then cured in an oven at 75°C for 1 hour. The coated electrode was finally immersed in distilled water for up to 10 day to obtain a stable and reproducible response.

Electrode Response Measurement

Electrochemical impedance spectroscopy (EIS) was performed at open circuit potential (OCP) using a Solartron 1286 Electrochemical Interface coupled with a Solartron 1255 Frequency Response Analyzer (FRA). A 10 mV ac amplitude sine wave excitation and a frequency range from 10^5 to 10^{-1} Hz were used. The OCP of the wire was monitored with the potentiostat and calibrated vs. the pH measured using a Thermo Orion™ glass electrode and a bench top Oaklon™ pH meter.

Results and Discussion

Figure 1a shows the current-potential response of the Ir wire as a function of the number of potential scans between +1.25 and 0 volts in 0.5 M sulfuric acid. While it has been well established that the peaks centered around 0.66 V originate from redox reactions between Ir(IV) and Ir(III) species, the stoichiometry of the oxides is not resolved and not investigated here. By comparing the current profile of the first cycle with the current profile of the 10th and 600th cycles, it was apparent that: (1) the Ir(IV)/Ir(II) redox peaks developed during the course of potential cycling test, and (2) the presence of Ir(IV) oxides reduced the current from water oxidation and hydrogen evolution. Additionally, it was observed that the increase in the intensity of the anodic and cathodic current peaks at 0.66 V leveled off with the increasing number of potential scans. Finally, the oxidation peak current at 0.66 V was always larger than the corresponding reduction peak (Figure 1b), which indicated that an iridium oxide layer was not quantitatively reduced during the course of the cyclic voltammetry experiment.

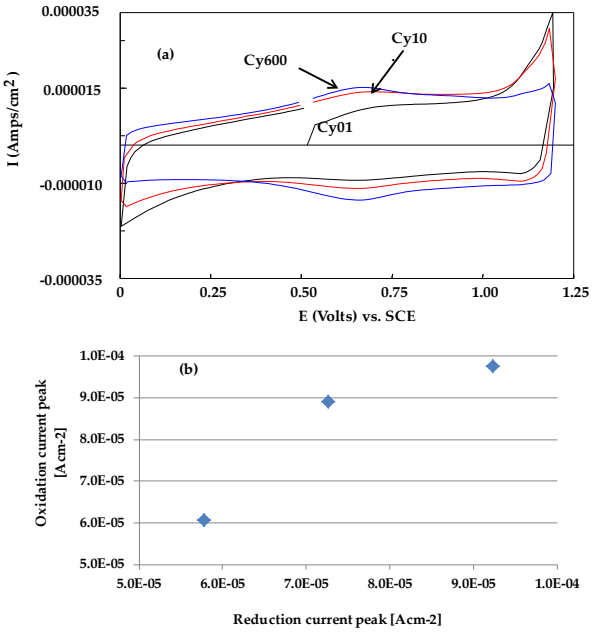

FIGURE 1. CYCLIC VOLTAMMOGRAM OF IRIDIUM IMMERSED IN (a) 0.5M H_2SO_4, AND (b) PLOT OF THE OXIDATION VS. REDUCTION CURRENT PEAK.

The effect of potential cycling was monitored by collecting electrochemical impedance spectra at open circuit potential (ca. 500 mV) as a function of the number of cycles as illustrated in Figure 2a and 2b. The Bode plots (Figure 2a and 2b) showed that a shift of the impedance magnitude and phase angle towards lower frequency resulted after electrode oxidation. Such changes are usually indicative of a variation of the interfacial capacitance. This was confirmed by Figure 2c where the electrode capacitance determined by least square fitting of the spectra to an equivalent circuit was plotted as a function of the number of potential cycles. The capacitance increased and leveled off with increasing number of cycles and over 90% of the capacitance change occurred within the first 100 cycles. This correlated with the cyclic voltammetry shown in Figure 1 where the peak current increase leveled off as the number of cycles increased. The capacitance increase was attributed to an increase in surface roughening due to the oxide formation rather than a pseudocapacitance for 2 two main reasons: first, because (1) the applied bias potential during the electrochemical impedance measurements was in a

non-Faradaic potential region and second, because the measured capacitance was two orders of magnitude lower than what is expected for a pseudocapacitance. The presence of a Nafion® coating did not cause any significant change in the impedance spectrum (Figure 3), which was an anticipated outcome given the excellent conducting properties of Nafion®.

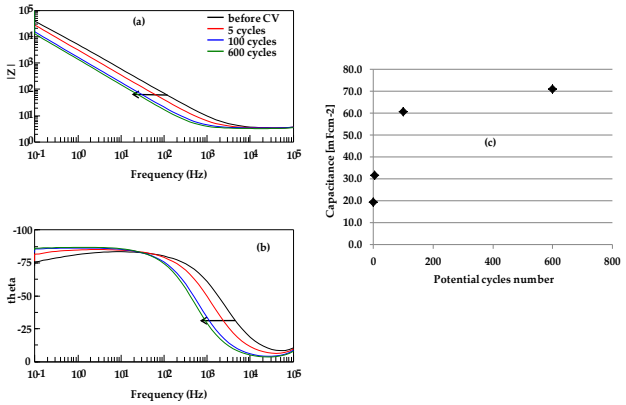

FIGURE 2. THE ELECTROCHEMICAL IMPEDANCE (a) MAGNITUDE AND (b) PHASE ANGLE PLOT OF IRIDIUM AT DIFFERENT OXIDATION STEPS. (c) THE ELECTRODE INTERFACIAL CAPACITANCE AS A FUNCTION OF THE NUMBER OF POTENTIAL CYCLES.

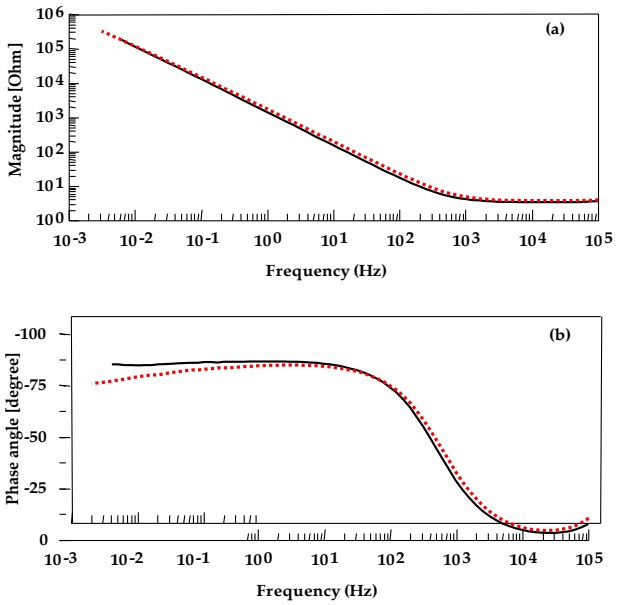

FIGURE 3. THE ELECTROCHEMICAL IMPEDANCE (a) MAGNITUDE AND (b) PHASE ANGLE PLOT OF OXIDIZED UNCOATED (DOTTED LINE) AND NAFION® COATED (SOLID LINE) IRIDIUM ELECTRODE.

A large amount of research has been conducted on the study of the iridium oxide species involved in the electro-oxidation of the metal. The iridium oxides are assumed to be hydrated oxyhydroxides and Table 1 reports some of the possible species that can be formed. When the mechanism for the reduction of Ir(IV) to Ir(III) involves the participation of one proton, the potential changes by 59 mV per pH unit. However, since the hydroxylated oxides are amphoteric species, the experimental pH dependence of the electrode potential may be dramatically different from 59 mV/pH as illustrated by the following example:

$$Ir_2O(OH)_6 + 2e + 2H^+ = 2Ir(OH)_3 + H_2O \quad (1)$$

If the hydroxo-Ir(III) species partially dissociate according to the following equilibrium

$$Ir(OH)_3 = Ir(OH)_2O^- + H^+ \quad (2)$$

Reaction 1 can be written as

$$Ir_2O(OH)_6 + 2e + 2H^+ = Ir(OH)_3 + Ir(OH)_2O^- + H^+ + H_2O$$

which can be simplified to

$$Ir_2O(OH)_6 + 2e + H^+ = Ir(OH)_3 + Ir(OH)_2O^- + H_2O \quad (3)$$

When the Nernst equation is applied to the equilibrium reaction (3), a potential/pH dependence of about 30 mV per pH unit is obtained. Similarly, slopes larger than 59 mV/pH are not unusual in the literature. Based on these considerations, it follows that conditioning the iridium oxides in water is a critical step in the preparation of the pH sensor, and immersion in distilled water for up to 10 days is necessary for stabilization of the pH sensor presented here.

TABLE 1. LIST OF POSSIBLE Ir(III) AND Ir(IV) OXIDES AND HYDROXIDES .

Ir(III) Species	Ir(IV) Species
IrO(OH)	IrO_2
$Ir(OH)_3$	$IrO(OH)_2$
Ir_3O_3	$Ir(OH)_4$
$Ir_2O(OH)_4$	$Ir_3OH_3(OH)_2$
	$Ir_2O(OH)_6$

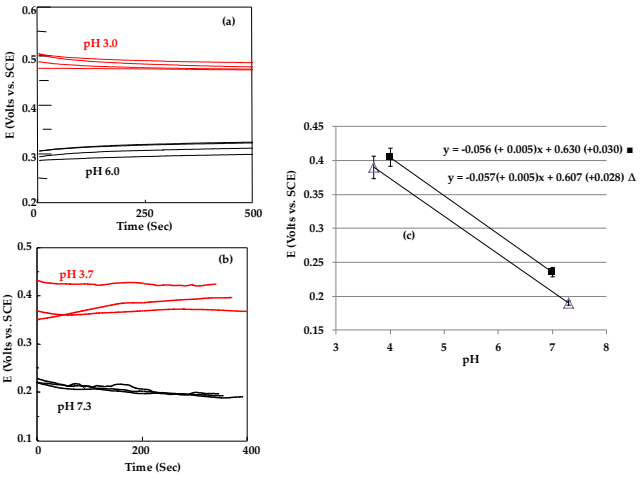

FIGURE 4. (a) TWO POINT CALIBRATION OF THE IRIDIUM SENSOR IN INORGANIC BUFFER SOLUTIONS, (b) FETAL BOVINE SERUM, AND (c) CORRESPONDING CALIBRATION CURVES. SERUM Δ, INORGANIC BUFFERS ■.

When the Nafion®-coated Ir electrode was calibrated in inorganic buffered solutions, a potential-pH relationship was obtained where the potential decreased by 56 ±5 mV per pH unit with increasing pH (Figure 4a). When the electrode was immersed in protein-containing environments such as fetal bovine serum, the potential response of the pH sensor had the same sensitivity (57 ±5 mV/pH), but shifted to more negative potential values as shown in Figure 4. The systematic negative shift of the potential observed in biological solutions was attributed to a decrease in the efficiency with which Nafion® conducts protons. The authors postulated here that the polymeric membrane interacted with the organic matter present in the biological medium, which partially blocked the sulfonic groups responsible for proton mobility across the Nafion® film.

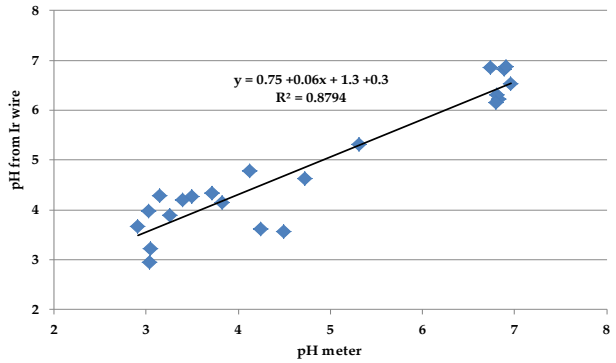

FIGURE 5. CORRELATION BETWEEN THE PH OF CELL CULTURE MEDIA OBTAINED USING A COMMERCIAL GLASS ELECTRODE AND THE PH MEASURED WITH THE Ir WIRE CALIBRATED IN SERUM.

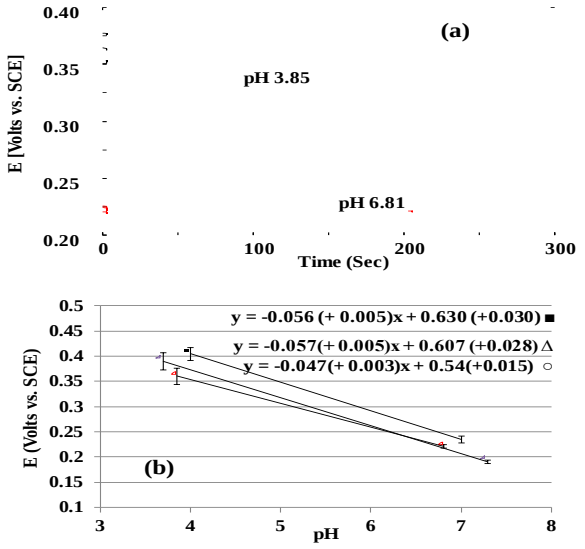

FIGURE 6. POTENTIAL CHANGE OF IRIDIUM SENSOR IN ARTIFICIAL SALIVA AS A FUNCTION OF pH (a) AND COMPARISON BETWEEN THE CALIBRATION CURVE OBTAINED IN INORGANIC BUFFERS (■), SERUM (Δ) AND SALIVA (○).

It was preliminarily concluded that to successfully test the pH of a biological environment, it was necessary to: (1) use a proton conducting polymer such as Nafion® to protect the underlying iridium oxide from interaction with proteins, and (2) calibrate the pH sensor in serum. Figure 5 shows the correlation between the pH of oral biofilm culture media measured with the iridium sensor calibrated in serum and a commercial glass pH electrode. Since the sensor will eventually be used for pH measurements of oral biofilms, it was also calibrated in artificial saliva as shown in Figure 6. As illustrated by Figure 6a, the electrode potential reached stability after ca. 50 seconds. In addition, Figure 6b showed that the calibration in artificial saliva resembled the results obtained in serum, which confirmed that a proteinaceous environment caused the potential readings to be shifted in the negative direction. However, the pH sensitivity was reduced to 47±3 mV/pH. It was unclear why the pH sensitivity was lower in artificial saliva. It was possible that the amphoteric nature of iridium oxide was affected by the electrolyte, but further studies are needed to clarify this finding. The correlation between the pH of cell culture media measured with the iridium sensor calibrated in artificial saliva and a glass pH meter is reported in Figure 7. The goodness of the correlation is comparable with that obtained with a serum calibration (Figure 5) as indicated by similar linear regression coefficients. The linear correlations shown in Figure 5 and Figure 7 were obtained after an electrode conditioning time of 276 hours. This long conditioning time was attributed to the thickness of the Nafion® film when using a 5% Nafion® solution. Therefore, in order to improve the performance and reduce the conditioning time, the use of a more diluted Nafion® solution (2.5% vs. 5.0% solution) was tried in the preparation of the electrode. Figure 8a and 8b show the response of the pH sensor after calibration in artificial saliva and a conditioning time of 42 and 72 hours respectively. As indicated by the correlation coefficient, a significant improvement in the performance of the sensor response vs. the glass electrode was obtained after only 42 hours conditioning when using 2.5% Nafion® solution (Figure 8a). However, some deterioration of the electrode performance was observed after 72 hours (Figure 8b).

In order to further test the response of the iridium pH sensor, an experiment was conducted where the pH of oral culture media was concomitantly monitored by a glass electrode and the iridium sensor. Additions of concentrated sodium hydroxide and formic acid were

used to change the pH *in situ* while stirring the solution. Such experiments tried to simulate the actual application of the iridium sensor where the coated wire is used *in situ* to monitor the pH of oral biofilms over time. Oral microorganisms are known to change the pH locally, but quantitative pH measurements within the microbial colonies have been difficult to date. Figure 9 reports the results of the *in-situ* pH test measurement where the time variation of the potential of the iridium electrode was reported in conjunction with the pH values recorded with a glass electrode after the addition of the concentrated acid and base. As shown in Figure 9, the iridium potential promptly changed depending on whether the solution was acidified or neutralized. Figure 10 shows the corresponding calibration curves obtained when plotting the wire potential vs. the pH measured with the glass electrode. The sensitivity of the sensor was 46 mV/pH after 24 hours conditioning in water. The linear correlation obtained from the *in situ* test was very promising because not only could the sensor demonstrate if a biofilm pH was above or below the critical pH threshold for caries initiation (pH 5.5), but it could also provide for the first time, quantitative data on the local pH existing underneath oral biofilms.

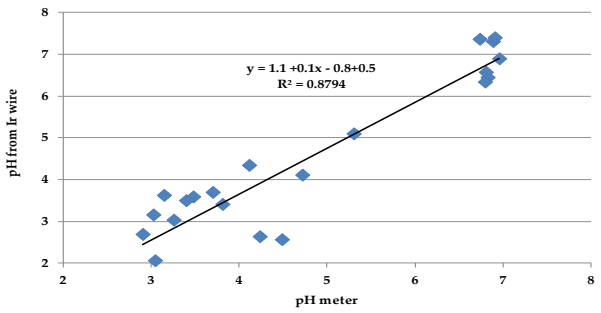

FIGURE 7. CORRELATION BETWEEN pH THE GLASS ELECTRODE RESPONSE AND MEASURED WITH THE Ir CALIBRATED IN SERUM AND SALIVA. THE pH OF ORAL BIOFILMS CULTURE MEDIA WAS ASSESSED.

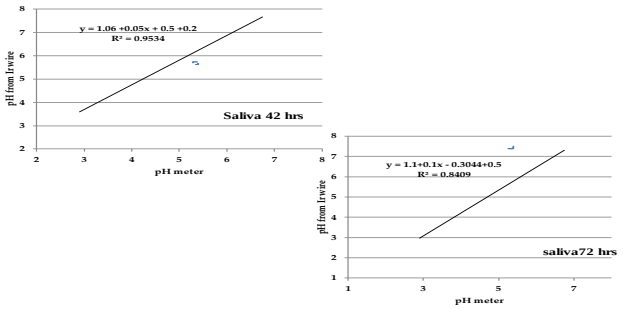

FIGURE 8. CORRELATION BETWEEN THE RESPONSE OF A COMMERCIAL pH METER AND THE IRIDIUM SENSOR PREPARED WITH A 2.5% NAFION SOLUTION AND CONDITIONED IN WATER FOR 42 AND 72 HOURS. THE pH OF ORAL BIOFILMS CULTURE MEDIA WAS ASSESSED.

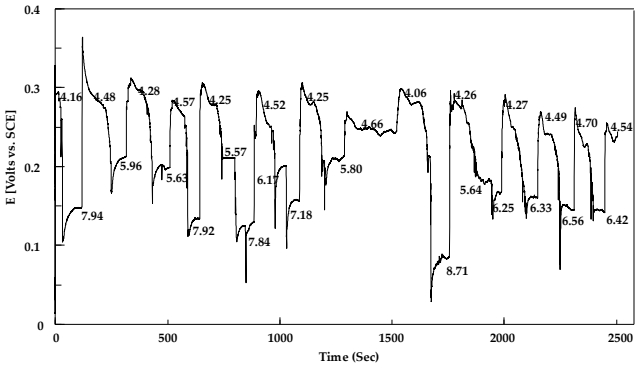

FIGURE 9. TIME DEPENDENCE OF THE POTENTIAL OF AN IRIDIUM WIRE CALIBRATED IN ARTIFICIAL SALIVA. PH WAS CHANGED IN SITU AND CONCOMITANTLY MONITORED WITH A GLASS ELECTRODE. A CONDITIONING TIME OF 24 HOURS AND 2.5% NAFION SOLUTION WERE USED.

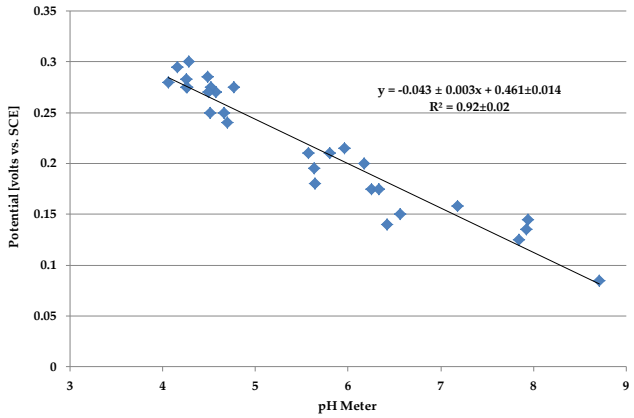

FIGURE 10. CALIBRATION OF THE NAFION COATED IRIDIUM SENSOR RESULTING FROM THE *IN SITU* TEST SHOWN IN FIGURE 9.

Conclusions

A miniaturized iridium pH sensor was calibrated for biological applications; and it was shown that: (1) a calibration in proteinaceous solutions was necessary before testing in biological media, (2) the use of thin Nafion® coatings led to reduced electrode conditioning times and (3) a sensitivity lower than 59 mV/pH was obtained.

ACKNOWLEDGMENTS

This work was supported by the National Institutes of Health's National Institute of Dental and Craniofacial Research under contract No.1R01 DE 21394-01.

Professor Heidi B. Kaplan form the Medical School of the University of Texas Health Science Center is thanked for providing the spent cell culture media.

REFERENCE

A. Alentiev; J. kostina; G. Bondarenko. Chemical Aging of

Nafion: FTIR Study. Desalination, 200, 2006, 32 – 33.

A. Fog; R Buck. Electronic Semiconductor Oxides as pH Sensors. Sensor Actuator 5, 1984, 137 – 146.

A. N. Bezbauruah, T C. Zhang, fabrication of Anodically Electrodeposited Iridium Oxide Film pH Microselectrodes for Microenvironmental Studies, Anal. Chem. 2002, 74, 5726-5733.

C. W. Pan; J.C. Chou; T.P. Sunand; SK Hsiung. Development of the Tin Oxide pH Electrode by the Sputtering Method. Sensor Actuat B-Chem, 108, 2005, 863 – 869.

D. O'Hare; K. H. Parker; C. P. Winlove. Metal-Metal Oxide pH Sensors for Physiological Applications. Med Eng Phys, 28, 2006, 982 – 988.

E. Kinoshita, F. Ingman, G. Edwall, S. Thulin, Polycsystalline and Monocrystalline Antimopny, Iridium and Palladium as Electrode Material for pH Sensing Electrodes. Talanta, vol. 33, No 2, 1986, 125-134,

F. Moussy, D. J. Harrison, Prevention of the Rapid Degradation of Subcutaneously Implanted Ag/AgCl reference Electrodes Using Polymer Coatings. Aanal. Chem. 1994, 66, 674-679.

H. Galster. pH Measurements – Fundamentals, Methods, Applications, Instruments. VCH Publishers, New York, 1991.

J. E. Baur; T. W. Spaine. Electrochemical Deposition of Iridium (IV) Oxide from Alkaline Solutions of Iridium (III) Oxide. J Electroanal Chem, 443, 1998, 208 – 216.

K. Yamanaka. Anodically Electrodeposited Iridium Oxide Films (AEIROF) from Alkaline Solutions for Electrochromic Display Devices. Jpn J Appl Phys, 28, 1989, 632 – 637.

K. A. Mauritz; R. B. Moore. State of Understanding of Nafion. Chem. Rev., 104, 2004, 4535 – 4585.

K. G. Kreider; M. J. Tarlov; J.P. Cline. Sputtered Thin-Film pH Electrodes of Platinum, Palladium, Ruthenium, and Iridium Oxides. Sensor Actuat B-Chem, 28, 1995, 167 – 172.

L. D. Burke, J. K. Mulcahy, D. P. Whelan, Preparation of an Oxidized Iridium Electrode and the Variation of its Potential with pH. J Electroanal. Chem., 163, 1984, 117-128.

M. Wang; S. Yao; M. Madou. A Long-term Stable Iridium Oxide pH Electrode. Sensor Actuat B-Chem, 81, 2002, 313 – 315.

M. J. Tarlov, S. semancik, K.G. Kreider, Mechanistic and Response Study of Iridium Oxide pH Sensors, Sensors and Actuators B , 1, 1990, 293-297.

M. P. Pechini, USA Patent, no. 3.330.697, July, 1967.

P. Steegstra, E. Ahlberg, Influence of Oxidation State on the pH Dependence of Hydrous Iridium Oxide Films, Electrochimica Acta, 76, 2012, 26-33.

S.M. Cobbe, PA Poole-Wilson, Catheter pH Electrodes for Continuus Intravascular Recordings. J Med Eng Tech, 41, 1980, 122 – 124.

W. Olthuis, M.A.A. Robben, P. Bergveld, pH Sensor Properties of Electrochemically Grown Iridium Oxide, Sensors and Actuators B, 2, 1990, 247-256.

W.D. Huang, H. Cao, S. Deb, M. Chiao, J.C. Chiao, A Flexible pH Sensor Based on the Iridium Oxide Sensing Film, Sensors and Actuators A 169 2011 1-11.

doi: 10.14355/ijmsci.2014.0401.03

Complexation of Cobalt with a Heteropolyanion of Dawson Type and Recovery by Emulsified Liquid Membrane

Nacéra Zabat*[1], Mostefa Abbessi[2]

Department of Process Engineering, Badji Mokhtar-Annaba University
P.O. Box 12, 23000, Annaba, Algeria

*[1]zabatnassira@yahoo.fr; [2]mostefa_abbessi@yahoo.fr

Abstract

In this study, a lacunar heteropolyanion (HPA) of Dawson type $(P_2W_{15}Mo_2O_{61})^{10-}$ was prepared and tested in the complexation of aqueous (Co^{2+}). The complex formed was recovered after that using an emulsified liquid membrane (ELM). The results showed that the complex $(P_2W_{15}Mo_2O_{61}Co)^{8-}$ was very stable with constant stability of $\beta = 4{,}073.10^3$. The recovery of this complex formed by (ELM) attained the yield of 70%.

Keywords

Polluted Water; Heavy Metals; Cobalt; Complexation; Heteropolyanions; Emulsified Liquid Membrane

Introduction

The qualitative and quantitative analysis of toxic metals likely to be present in water of industrial wastes generally requires a preliminary complexation. The ligand or sequestering agent must be selected according to its capacity to give a stable and easily identifiable complex. The ligand must have physico-chemical properties definitely different from those of the formed complex thus facilitating the possibility of checking this complexation of following evolution of this one. The lacunars Heteropolyanions of Dawson type [Dawson, 1953] lend themselves perfectly to addition reactions leading to mixed compounds [Ciabrini, 1993; Belghiche, 2002; Contan, 2004]. Thus the addition of transition metals leads to complexes of the form $(P_2W_{15}Mo_2O_{61}X)^{n}$ such as ($X=Co^{2+}$, Pb^{2+}, Fe^{2+}, Ni^{2+}, Cu^{2+}…). The mixed species, having electrochemical and electrocatalytic remarkable properties [Keita, 2001; Keita, 2005; Gkika, 2005], show very interesting applications in analytical chemistry [Keita, 1999], homogeneous and heterogeneous catalysis [Kholdeeva, 1992; Guo, 2007] and in field of electrochemical sensors [Zabat, 2008]. With the aim to check the possibilities of fixing a bivalent element, likely to be regarded as pollutant or to be used like catalyst, we studied the complexation of lead being in aqueous medium (Co^{2+}) by a ligand monovacant $(P_2W_{15}Mo_2O_{61})^{10-}$ in abrogated ($P_2W_{15}Mo_2$). The first part relates to the study of the factors influencing the stability of the complex $(P_2W_{15}Mo_2O_{61}\ Co)^{8-}$, such as pH, time, and on the determination of the stoechiometry and the constant of stability, by means of isomolaires series, saturation and balance displacement.

The second part treats the recovery of this formed complex, in order to subject it to the various methods of physicochemical analysis, by using the technique of extraction by emulsified liquid membrane. This technique is used as method of separation of compounds existing in water [Lin, 1999; Devulapalli, 1999; Kargari, 2004]. The liquid membrane of emulsion type constitutes also a separative technique of a great effectiveness for organically-aqueous liquid mixtures [HU, 2003; Wionczyk, 2004]. It corresponds to double emulsion water in oil in water (E/H/E) where the membrane separates the two adjacent aqueous phases of which is contaminated and another receiving. This technique taking the advantage to extract from made up with very weak concentrations requires a preliminary optimization of the independent factors which control it namely: Composition of the membrane (extractant, thinner, surfactant); pH of the external phase to extract; stirring velocity; ratio of organic phase on aqueous phase (O/A); ratio of volume of the external phase on the volume of the emulsion (Vext/Vemul); initial concentration of the external phase to extract.

Experimental

Preparation of Metallic Complex

The heteropolyanion $(P_2W_{15}Mo_2O_{61}Co)^{8-}$ was prepared by addition of cobalt nitrate on the lacunar compound

$(P_2W_{15}Mo_2O_{61})^{10-}$ based on methods described in the literature [Contant, 1997; Abbessi1989; Abbessi, 1991]. The monovacant compound $(P_2W_{15}Mo_2O_{61})^{10-}$ was obtained by reaction of addition of two molybdate MoO_4^{2-} on the trivacant compound (P_2W_{15}), this later was obtained by reaction of elimination of a tritungstic grouping which occupied the site "a" in the saturated species $\alpha P_2W_{18}O_{62}^{6-}$. The various structures of these heteropolyanions are presented in figure 1.

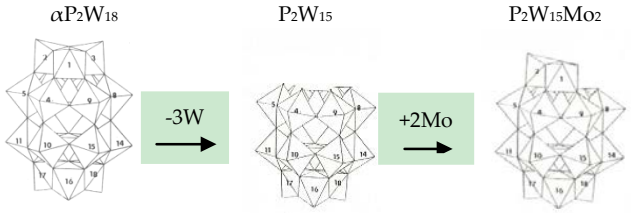

FIGURE 1. DIFFERENT STRUCTURES OF HETEROPOLYANIONS

Study of the Formation of Metallic Complex

Before extracting the complex $(P_2W_{15}Mo_2O_{61}Co)^{8-}$ by emulsified liquid membrane, it is useful to study accesses its stability according to the pH, the time and to determine its constant of stability. The analysis was carried out with a spectrophotometer 6405 UV/VIS (JENWAY).

Stability of the Complex According to pH

A UV-Visible sweeping with different pH was carried out in order to choose the optimum pH for the complex $(P_2W_{15}Mo_2O_{61}Co)^{8-}$. In this case of the equimolaires solutions made up of ligand, metal and buffer were used. The results obtained for the complex $(P_2W_{15}Mo_2O_{61}Co)^{8-}$, with different pH, are gathered in table 1.

It is noticed that the degree of formation of the formed complex is deducted from the value of the recorded maximum absorptance. The formation of the complex is very weak in acid medium; on the other hand, the basic medium is more favorable to its formation. The optimal pH for the formed complex $(P_2W_{15}Mo_2O_{61}Co)^{8-}$ is pH= 9 with a maximum wavelength λ_{max} =304 nm.

TABLE 1. INFLUENCE OF pH ON THE COMPLEX $(P_2W_{15}Mo_2Co)^{8-}$

pH	3	4	5	9	10	11
Absorptance	0,1840	0,1380	0,2798	0,8900	0,6419	0,8564
λ_{max}(nm)	301	316	314	304	302	301

Stability of the Complex According to Time

To determine the time for which the complex is stabilized, the variation of the absorptance according to the time was followed (Figure. 2).

The result reveals that the formed complex is stable in a rather broad time interval (one hour).

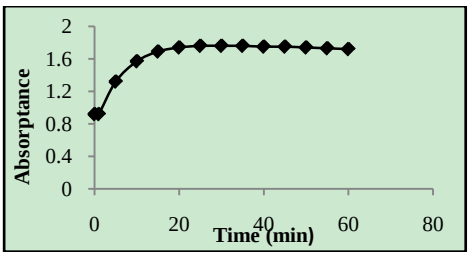

FIGURE 2. VARIATION OF THE ABSORPTANCE OF THE COMPLEX $(P_2W_{15}Mo_2Co)^{8-}$ ACCORDING TO THE TIME

Determination of the Constant of Stability of the Complex

The determination of the constant of stability was carried out by using statistical methods of calculation (method of isomolaires series, method of saturation and method of balance displacement) [Hamlaoui, 1990]

1) Method of Isomolaires Series

In this method, the volume of the buffer solution (pH=9) is maintained constant whereas the volumes of the solutions of ligand and cobalt, of the same concentration (5.10^{-4}M) are mixed in variable proportions in order to keep constant total volume.

According to the principle of the method of isomolaires series, the stoechiometry is deduced from report C_L/C_M leading to the maximum value of the absorptance. The result shows that the stoechiometry of the formed complex is equal to 1(figure. 3).

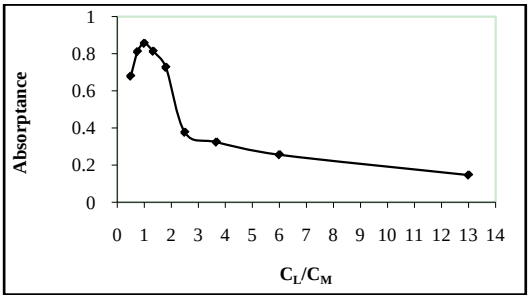

FIGURE 3. VARIATION OF THE ABSORPTANCE OF THE COMPLEX $(P_2W_{15}Mo_2Co)^{8}$ ACCORDING TO THE REPORT C_L/C_M BY MEHOD OF ISOMOLAIRE SERIES

2) Method of Saturation

This method consists in varying volumes of the ligands and the buffer solution, and maintains the volume of constant metal. Total volume is kept constant. The values of this method become source data in calculation of the constant of stability by the means of balance displacement.

The results represented in figure 4 showed that the

intersection of the tangents of the two parts of the curves (left ascending and the stage) makes it possible to deduce stoechiometry from the reaction which indicates the ratio C_L/C_M close to 1.

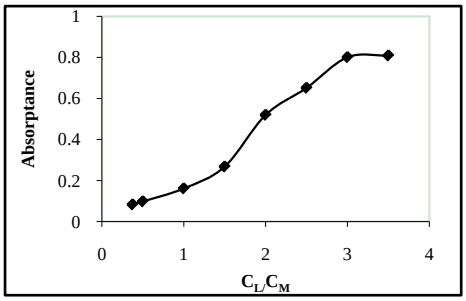

FIGURE 4. VARIATION OF THE ABSORPTANCE OF THE COMPLEX $(P_2W_{15}Mo_2Co)^{8-}$ ACCORDING TO THE REPORT C_L/C_M BY METHOD OF SATURATION

3) Method of Balance Displacement

The stoechiometry and constant of stability of the formed complex are determined by the method of displacement of balance based on the study of the linear dependence of the Equation (1):

$$log\ (Ai/Amax - Ai) = n log C_{Li} + log\ \beta \quad (1)$$

A_i: absorptance of the complex corresponding to the increasing part of the curve of saturation.

A_{max}: maximum absorptance corresponding to the stage of the curve of saturation.

n: stoechiometric report (C_L/C_M).

C_{Li}: concentration of the ligand correspondent to each value of A.

β: constant of stability.

By tracing Log (Ai/Amax - Ai) according to $LogC_{Li}$ for three points of the ascending part of the curve of saturation, figure 5 was plotted.

The stoechiometry of the complex $(P_2W_{15}Mo_2O_{61}Co)^{8-}$determined based on the graph(Figure.5) is equal to 1. The value of Log β is deduced also from this graph (log β = 3,610) from where β = $4,073.10^3$ thus revealing a sufficiently stable compound.

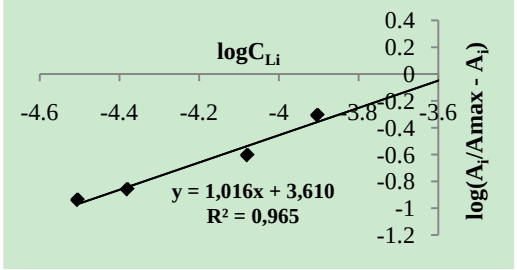

FIGURE 5. VARIATION OF $logC_{Li}$ ACCORDING TO LOG (Ai/Amax - A) FOR THE COMPLEX $(P_2W_{15}Mo_2Co)^{8-}$

Recovery of the Complex Formed $(P_2W_{15}Mo_2O_{61}Pb)^{8-}$ by Emulsified Liquid Membrane

1) Preparation of the Emulsified Liquid Membrane

The membrane intended to extract the complex $(P_2W_{15}Mo_2O_{61}Co)^{8-}$ was prepared with a mixture of extractant triethylamine $(C_2H_5)_3N$ (Aldrich) of thinner n-heptane (Riedel-in Hean) and surfactant monoleate of sorbitane SPAN80 (Federated) [Samar,1992]. The choice of the nature of extractant, the thinner and surfactant was made leave a bibliography search [Bourenane, 2003; Frites,2005].

For favorite emulsion water in oil (W/O), this emulsion was prepared by mixing a volume of the internal NaOH phase (0,2M) with a volume of the liquid membrane. The mixture was agitated at a number of revolutions of 5000 tr/min during 5 min with the aid of a homogenizer models ULTRA-TURRAX T 18-10. A stable emulsion was obtained.

2) Procedure of the Etraction by Emulsified Liquid Membrane:

To extract the complex considered, it was as follows: A volume of the membrane was taken and dispersed in a beaker containing 200 ml solution to be treated (external phase), whose initial concentration of the complex to be extracted is equal to 100 ppm. The mixture was agitated using a mechanical agitator (type RW20 Kjank & Kunkel). The pH evolution of the external phase was followed by means of a pH meter (type HANA Hi 8519N). In order to follow the variation of the Kinetics of extraction of the complex formed, $(P_2W_{15}Mo_2O_{61}Co)^{8-}$according to time, was carried out to takeg away of the external phase for following times of contact: (2, 4, 6 and 8min). After filtration, these samples were proportioned by a spectrophotometer 6405 UV/VIS (JENWAY).

The experimental study carried out described the evolution of the yield of extraction in function of a variety of parameters. This yield is calculated by the following formula:

$$Y_{ext} = C_{oext}.\ V_{oext} - C_{fext}.\ V_{fext}/C_{oext}.\ V_{oext} \quad (2)$$

C_{oext}= initial Concentration of the aqueous solution in the external phase

C_{fext}= final Concentration of the aqueous solution in the external phase

V_{oext}=initial volume of the aqueous solution in the external phase

V_{fext}= final Volume of the aqueous solution in the external phase

Results and Discussion

Optimization of Extraction Parameters

All the parameters are maintained constant except the parameter to optimize.

Operatories conditions

- Emulsification rate: 5000 revs/min;
- Emulsification time: 5 min;
- Temperature: 25°C;
- Concentration of internal phase (NaOH): 0,2 M;
- Concentration of external aqueous phase (solution to treat): 100 ppm;
- pH of the external phase: 9;
- Stirring velocity: 250 revs/min;
- Ratio of the organic phase on the internal phase (O/A)= 1;
- Ratio of the external phase volume on the emulsion volume (Vext/Vemul) =1.

1) Composition of the Membrane

Mass of Extractant. The Variation of the mass percentage of extractant varied automatically the composition of the membrane. The compositions of triethylamine, SPAN80 and n-heptane studied are: (15%, 12,5% and 72,5%); (25%, 12,5% and 62,5%); (30%, 12,5% and 57,5%); (35%,12,5% and 52,5%).

The experimental results are illustrated in figures 6 and 7.

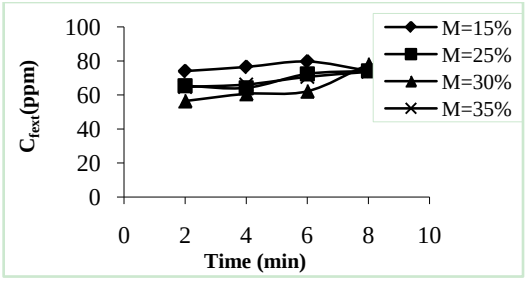

FIGURE .6 INFLUENCE OF MASS PERCENTAGE OF THE EXTRACTANT ON THE KINETICS OF EXTRACTION

Results showed that the optimal percentage of extractant in the membrane is 30% which corresponds to the best performance (Yext= 44%). Beyond, this percentage yield of extraction decreases. This can be explained by the fact why the increase in the mass of extractant destabilizes the emulsion and supports the emulsion oils in water. For percentages of extractant lower than 30%, yield also decreases, probably for that the mass of extractant is less important to extract the aqueous solution.

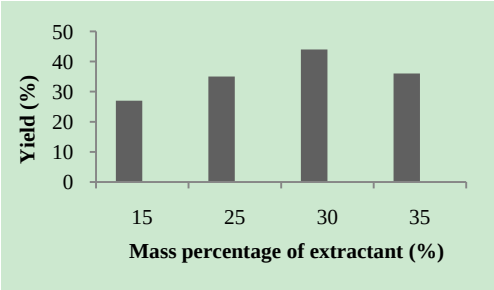

FIGURE.7. EFFECT OF MASS PERCENTAGE OF THE EXTRACTANT ON THE YIELD OF EXTRACTION

Mass of Surfactant. The parameters optimized previously are kept constant and the membranes were prepared with various percentages from surfactant which are the following: 12,5%,15%,25% and 35%.

Results indicate that the percentage of surfactant (Fig. 9) giving the best yield (Yext= 44%) is 12,5%. For values higher than 12,5%, the yield decreases. It seems that the membrane becomes very thick, which slows down the kinetics of extraction (Fig. 8).

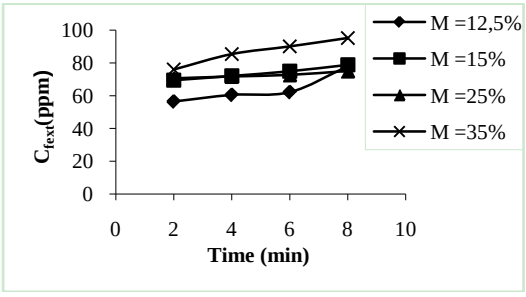

FIGURE. 8. INFLUENCE OF THE MASS PERCENTAGE OF SURFACTANT ON THE KINETICS OF EXTRACTION

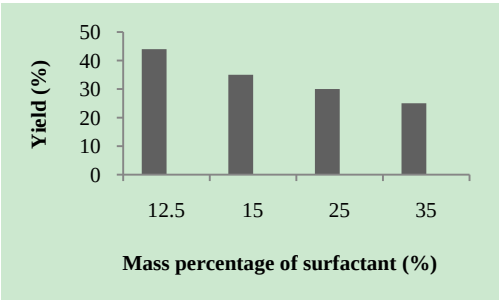

FIGURE .9. EFFECT OF MASS PERCENTAGE OF THE SURFACTANT ON THE YIELD OF EXTRACTION

2) pH of External Phase

The kinetics of extraction of the metallic complex was studied according to the different pH (fig.10). It is noticed that the best yield of extraction is (Yext=44%) obtained for pH=9 (fig.11). For the pH lower than 9, the yield of extraction decreases. This can be explained by the fact that in acid medium

the extractant which is an amine becomes degraded after a reaction with medium.

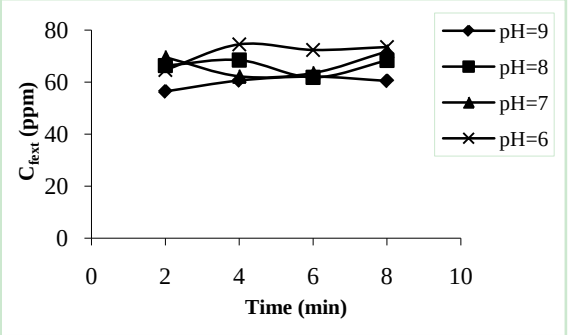

FIGURE. 10. INFLUENCE OF PH ON THE KINETICS OF EXTRACTION

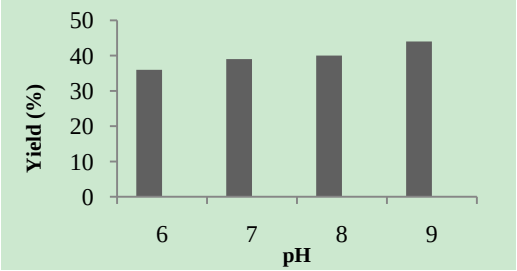

FIGURE 11. EFFECT OF PH ON THE YIELD OF EXTRACTION

3) *Stirring Velocity*

The stirring velocities used are: 100, 200, 250, 300, and 350 revs/ min.

Results of the stirring velocity influence on the kinetics are represented in figure 12.

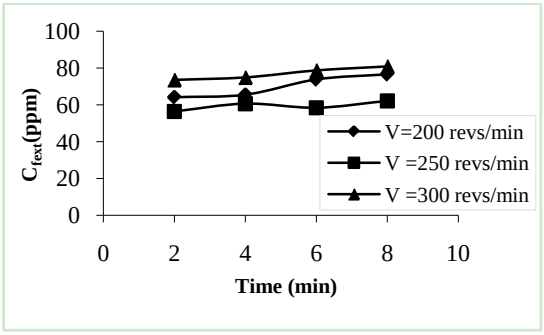

FIGURE. 12. INFLUENCE OF STIRRING VELOCITY ON THE KINETICS OF EXTRACTION

It was noted that the best yield (Fig.13) of extraction (Yext=44%) is obtained for a stirring velocity equal to 250 revs/min after 2 min of contact. Beyond this speed, the yield of extraction decreases, probably because of an important shearing caused by agitation, thus involving the rupture of the emulsion from which the expulsion of the aqueous solution already extracted the internal phase towards the external phase. This phenomenon affects the stability of the emulsion and increases the osmotic swelling of the membrane and makes the emulsion unstable [Yan,2001]. Below this optimal speed, the yield of extraction decreases because of the bad transfer of the aqueous solution following slow kinetics of extraction.

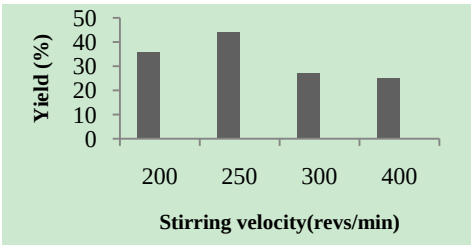

FIGURE 13. EFFECT OF STIRRING VELOCITY ON THE YIELD OF EXTRACTION

4) *Ratio of the Organic Phase on the Internal Phase (O/A)*

Different values from 0,5 to 3 of O/A ratio have been studied. Results of the influence of the O/A ratio on the kinetics of extraction are represented by curves in Fig. 14 and the yield in Fig. 15.

Results showed that the extraction is bad for the ratio of O/A lower than unit and it is worse for the ratio O/A higher than unit. This phenomenon can be explained by the fact that more volume of emulsion increases more the membrane becomes thick thus involving an increase in the viscosity of the emulsion, consequently, the aqueous solution to be extracted diffuses with difficulty through the membrane. The optimal ratio (O/A=1) is obtained for yield of extraction (Yext= 44%) at a time of contact equal to 2 min.

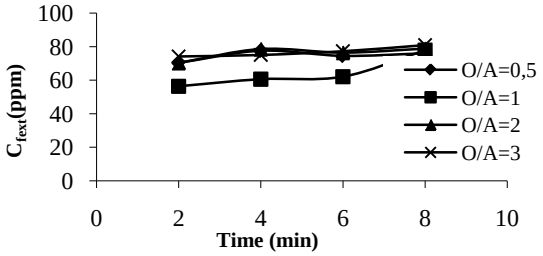

FIGURE 14. INFLUENCE OF RATIO O/A ON THE KINETICS OF EXTRACTION

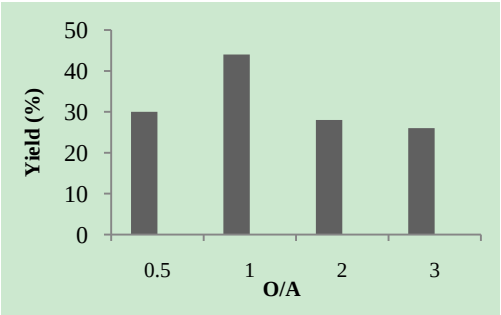

FIGURE .15. EFFECT OF RATIO O/A ON THE YIELD OF EXTRACTION

5) Ratio of the External Phase Volume on the Emulsion Volume (Vext/Vemul)

In order to study the influence of the ratio (Vext/Vemul) on the kinetic (Fig. 16) and yield of extraction (Fig. 17), the ratios varying from 5 to 15 were used. It is observed that for a report Vext/Vemul higher than 10, the extraction of metallic complex is less effective. This can be due to the volume of the external phase which increases and with the decreasing volume of emulsion, consequently, the mass of extractant becomes less important to extract the aqueous solution. If the ratio Vext/Vemul is lower than 10, the extraction is even less effective, probably because of the emulsion volume which is more important than that of the external phase that involves more thickness of the membrane film, therefore, a kinetic of extraction becomes low. The optimal ratio is Vext/Vemul=10 gives the best yield (Yext= 44%).

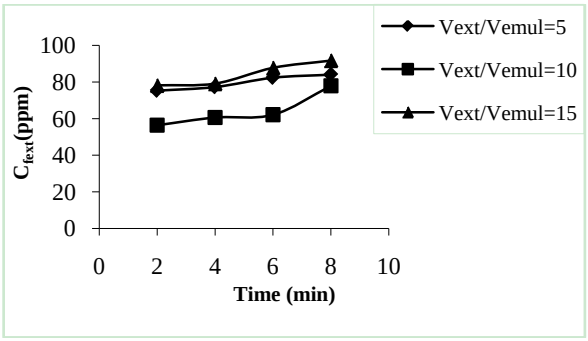

FIGURE 16. INFLUENCE OF THE Vext/Vemul RATIO ON THE KINETICS OF EXTRACTION

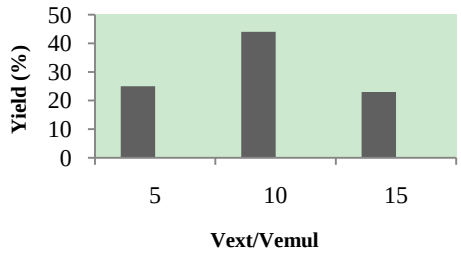

FIGURE 17. EFFECT OF RATIO Vext/Vemul ON THE YIELD OF EXTRACTION

6) Initial Concentration of the External Phase

This study was carried out by fixing the optimal parameters found previously and by varying the initial concentration of the external phase to extract: 50 ppm, 100 ppm and 150 ppm.

Results of the kinetics of extraction are illustrated in Figure. 18 and the yield in Figure. 19.

These figures indicate that when the initial concentration of the complex in the external aqueous phase is lower than 100 ppm, the extraction gives an important yield. For a concentration generally higher than 100 ppm, the extraction is unsatisfactory. The best yield of extraction (Yext= 70%) is obtained for an optimal initial concentration equal to 50 ppm for a time of contact equal to 4 min; which confirms the theory stipulating that one of the advantages of the emulsified liquid membranes is their use for much diluted concentrations.

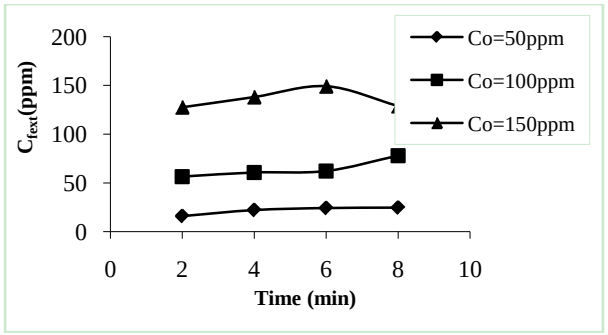

FIGURE 18. INFLUENCE OF THE INITIAL CONCENTRATIONS OF EXTERNAL PHASE ON THE KINETICS OF EXTRACTION

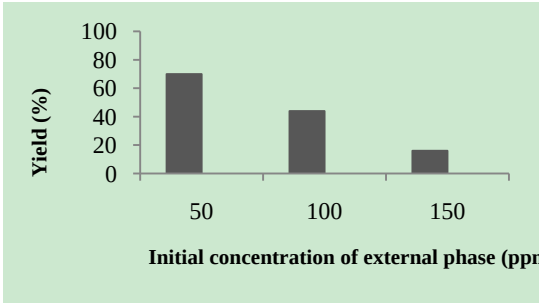

FIGURE 19. EFFECT OF THE INITIAL CONCENTRATION OF EXTERNAL PHASE ON THE YIELD OF EXTRACTION

7) Description of the Mechanism of Transport Through the Emulsified Liquid Membrane

To recover the complexe (aqueous solution) by emulsified liquid membrane (ELM), a mechanism of aqueous solution-extractant transport is described, for better understanding its chemical reaction with the interface of the membrane. The mechanism proposed is the following:

$$\overline{R_3N} + \overline{OH^-} \longrightarrow \overline{(R_3N, OH^-)}$$

$$8(R_3N, OH^-) + \overline{(HPACo)^{8-}} \longrightarrow \overline{(R_3N)_8\,(HPACo)} + 8OH^-$$

R_3N: Extactant (triethylamine)

HPA: $P_2W_{15}Mo_2O_{61}$

OH^-: basic medium where the extraction is favored, moreover the complex $(P_2W_{15}Mo_2O_{61}Co)^{8-}$ is stable in this pH=9 medium.

The mechanism of transport of the heteropolyanion

through the emulsified liquid membrane is schematized according to figure 20.

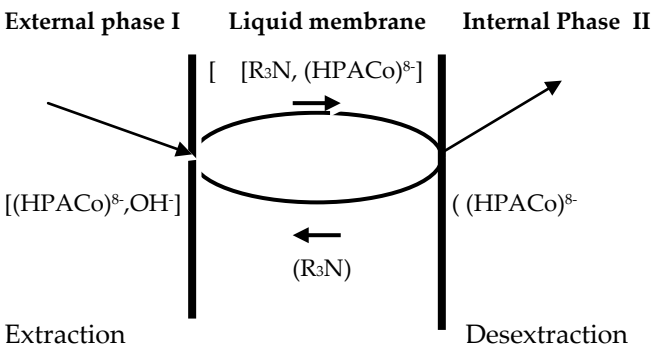

FIGURE 20. MECHANISM OF TRANSPORT OF HETEROPOLYANION THROUGH THE EMULSIFIED LIQUID MEMBRANE

Conclusion

The lacunar heteropolyanion prepared $(P_2W_{15}Mo_2O_{61})^{10-}$ seems to have remarkable properties of complexation. Of this fact, it can be used in the field of water treatment to fix toxic metals, as used in catalytic reaction as well as proposed in chemical analysis. This is confirmed by the analysis of spectra IR of the prepared complex, showing that the metal element (Co^{2+}) is in the vicinity of the gap of the ligand $(P_2W_{15}Mo_2O_{61})^{10-}$. Moreover, the constant of given stability indicates the use potential of this compound, particularly in aqueous mediums, without risk of decomposition. Indeed, the constant of stability is rather high; which is equal to $\beta = 4{,}073.10^3$.

The extraction by emulsified liquid membrane of the complex $(P_2W_{15}Mo_2O_{61}Co)^{8-}$ which could serve with effective manner in the electrocatalytic reduction of nitrates in a slightly acid solution, was the object of this work. The study of membrane made up of SPAN80 as surfactant and TEA as extractant according to the various parameters, showed that the increase in the concentration of extractant and surfactant stabilizes the emulsion. The increase in the pH of medium (basic pH), favorites the extraction of complex. The increase of the stirring velocity would cause a shearing and the phenomenon of osmosis (swelling). The increase in O/A ratio involves an increase in the viscosity of the emulsion. The increase in Vext/Vemul ratio would cause the instability of the membrane. It has been found that the parameter of the initial concentration of the external phase plays an important role in improving the extraction yield. Hence, the decrease of the initial concentration of the external phase significantly increased the extraction yield, rising from 44% (Co=100ppm) to 70% (Co=50ppm). It was deduced then that the extraction by ELM is favored for very dilute concentrations of the external phase.

The yield of extraction for the complex formed $(P_2W_{15}Mo_2O_{61}Co)^{8-}$ is of 70%; under the following optimal operating conditions:

- pH of the external phase to extract is equal to 9;
- Stirring velocity = 250 revs/min;
- Ratio O/A is equal to 1;
- Mass percentage of extractant in the membrane is 30%;
- Mass percentage of surfactant in the membrane is 12,5%;
- Ratio Vext/Vemul is equal to 10;
- Initial concentration of the external aqueous phase for the complex $(P_2W_{15}Mo_2O_{61}Co)^{8-}$ is equal to 50 ppm.

REFERENCES

Abbessi, M. «Synthèse et propriétés d'hétéropolyanions vanado- molybdo-tungsto-phosphoriques en vue d'une application en catalyse d'oxydation». Thèse de doctorat, Université de Paris, 1989.

Abbessi, M., Contant, R., Thouvenot, R., Hervé, G. "Dawson type hétéropolyanions. 1. Multinuclear (^{31}P,^{51}V,^{184}W) NMF structural investigations of octadeca (molybdotungstovanado) diphosphate". Inorg.Chem 30 (1991): 1695-1702.

Belghiche, R., Contant,R., Lu,Y.W., Keita,B., Abbessi, M., Nadjo,L., Mahuteau, J. "Synthesis and caracterization of Fe-or Cu-substituted molybdenum-enriched tungstodiphosphates". Eur.J.Inorg.Chem (2002): 1410-1414.

Bourenane, S., Samar, M.H., Abbaci, A. "Extraction of cobalt and lead from waste water using a liquid surfactant membrane emulsion". Acta Chim.Slov 51 (2003): 259-264.

Contant, R., Abbessi, M., Canny, J. Belhouari, A. Keita, B., Nadjo, L. Inorganic Chemistry 36 (1997): 4961-4967.

Contant,R., Abbessi,M., Thouvenot,R.,Hervé, G. "Dawson type heteropoyanion.3.Syntheses and ^{31}P, ^{51}V,and ^{183}WNMR Structural Investigation of Octadeca(molybdo-tungsto-vanadodiphosphates related to the $[H_2P_2W_{12}O_{48}]$ Anion". Inorg.Chem 43 (2004): 3597-3604.

Ciabrini, J.P., Contant, R. "Mixed heteropolyanions. Synthesis and formation constants of Cerium (III) and

Cerium (IV) complexes with lacunary tungstophosphates". J.Chem.Research 391 (1993): 2720-2744.

Dawson, B. "The structure of the 9(18)-heteropolyanion in potassium 9(18)-tungstophosphate,$K_6(P_2W_{18}O_{62}).14H_2O$". Acta. Crystallogr 6 (1953): 113.

Devulapalli, R., Jones, F. "Separation of aniline from aqueous solutions using emulsion liquid membranes". Journal of Hazardous Materials B 70 (1999): 157-170.

Frites, M., Samar, M. H., Boutefnouchet, N., Abbaci, A."Extraction of chromium(VI) from aqueous solution by liquid surfactant membrane". Asian Journal chemistry (2005): 1397-1405.

Gkika, E., Troupes, A., Hiskia, A., Papaconstantinou, E." Photocatalytic reduction of chromium and oxydation of organics by polyoxometalates". Applied Catalysis B: Environmental 62 (2005): 28-34.

Guo,Yihang., Hu, Changwen. "Heterogeneous photocatalysis by solid polyoxometalates". Journal of Molecular Catalysis". 262 (2007): 136-148.

Hamlaoui, M.L., Vlassenko, K., Messadi.D. "Constante de stabilité des complexes de quelques métaux de transition avec l'hétéropolyanion non saturé $[P_2W_{17}O_{61}]^{10-}$ " . C.R. Acad. Sci. Paris 311 (1990): 795-798.

HU, S. B., Li, J., Wiencek, J. "Feasibility of surfactant-free supported emulsion liquid membrane extraction". Journal of Colloid and Interface Science 266 (2003): 430-437.

Kargari, A., Kaghazchi, T., Soleimani, M. "Role of emulsifier in the extraction of gold (III) ions from aqueous solutions using the emulsion liquid membrane technique". Desalination 162 (2004): 237-247.

Keita, Bineta., Girard, Francois., Nadjo, Louis., Contant, Roland., Canny, Jacqueline., Richet, Martine. "Metal ion complexes derived from the α_1 isomer of $(P_2W_{17}O_{61})^{10-}$: comparison with the corresponding α_2 species". Journal of Electroanalytical Chemistry 478 (1999): 76-82.

Keita, B., Girard,F., Nadjo,L., Contant,R., Belghiche,R., Abbessi,M. "Chemistry, Cyclic voltammetric evidence of facilitation of the reduction of nitrite by the presence of molybdenum in Fe-or Cu-substituted heteroplytungstates". Journal of Electroanalytical 508 (2001): 70-80.

Keita, Bineta., Mbomekalle, Israel-Martyr., Nadjo, Louis., Oliveira,Pedro., Ranjbari, Alireza., Contant, Roland. "Vanadium-substituted Dawson-type polyoxometalates as versatile electrocatalysts". C.R.Chimie 8 (2005): 1057-1066.

Kholdeeva, A O., Golovin, A.V., Maksimovskaya, R.I., Kozhevnikov, I.V. "Oxidation of 2,3,6-trimethylphenol in the presence of molybdovanadophosphoric heteropoly acids". Journal of Molecular Catalysis 75 (1992): 235-244.

Lin, S.H., Pan, C.L., Leu, H.G. "Liquid membrane extraction of 2-chlorophenol from aqueous solution". Journal of Hazardous Materials B 65 (1999): 289-304.

Samar, M., Pareau, D., Chesne, A., Durand, G. « Membrane liquides échangeuses de cations: Application à l'extraction du nickel ». Bull Soc Chim Fr 129 (1992): 259-264.

Wionczyk, B., Apostoluk, W. "Solvent extraction of chromium (III) from alkaline media with quaternary ammonium compounds. PartI". Hydrometallurgy 72 (2004): 185-193.

Yan, J., Pal, R. "Osmotic swelling behaviour of globules W/O/W emulsion liquid membranes". J.Membr.Sci. 190 (2001) 79-9

Zabat, N., Abbessi, M., Kherrat, R., Jaffrezic-Renault, N. , Zougar, S., Grid, A. "Elaboration of Impedancemetric sensor for cobalt detection by polymeric membrane incorporating a heteropolyanion of Dawson type". Materials Science and Engineering C 28 (2008): 1006-1009.

doi: 10.14355/ijmsci.2014.0401.04

Acoustic Emission Based Method to Characterize Glass/Epoxy Composite Damages During 3-point Bending Test

Mohamad Fotouhi[1], Parinaz Belalpour Dastjerdi[*2], Mehdi Ahmadi[3]

Non-destructive Testing Lab, Department of Mechanical Engineering, Amirkabir University of Technology
424 Hafez Ave, 15914, Tehran, Iran

[1]fotouhi.mohamad@gmail.com; [*2]p.belalpour@aut.ac.ir; [3]ahmadin@aut.ac.ir

Abstract

Acoustic emission (AE) method is a capable non-destructive method for recognition of different fracture mechanisms in composite materials. Discrimination of AE signals related to various fracture modes is important in the application of this technique. Thus, in this study, integration of genetic algorithm (GA) and k-means algorithm was used to cluster AE signals of glass/epoxy composite during quasi-static three-point bending test. Performing clustering analysis, three clusters with distinct frequency ranges were obtained; and each one indicates a separate fracture mechanism. In addition, time-frequency analysis of AE signals, which is derived from wavelet packet transform (WPT), was performed. With the purpose of finding the principal components correlated with various damage mechanisms, the energy distribution criterion was used. The frequency ranges of the principal components were then compared with k-means genetic algorithm (KGA) results. Also, SEM observation was used to validate the results. The achieved results indicate excellent performance of the proposed techniques in the damage discrimination of composite materials.

Keywords

Acoustic Emission (AE); Glass/Epoxy Composite; Damage Characterization; Wavelet Packet Transform (WPT); k-means Genetic Algorithm

Introduction

Fiber-reinforced plastic (FRP) composite materials are widely utilized in many engineering fields due to their strength and high specific stiffness. In order to obtain the higher properties, composite materials are combined of two or more materials which vary in physical shape and chemical properties. Therefore, a variety of damage mechanisms may appear in the long-term performance of these materials. Delamination is one of the most important fracture mechanisms in composites due to its significant effect on the reduction of the fatigue life and residual strength. Therefore, its recognition is really an essential task. Some previous studies showed that the main types of damages in delamination of laminated composite materials are matrix cracking, fiber failure and etc. In order to recognize the main types of damages caused in delamination; matrix cracking, fiber failure and etc, AE is an efficient method which is the result of transient elastic wave propagation derived from a rapid release of energy within a material caused by changes in local stress and strain fields. These elastic waves cover audible frequencies and frequencies in MHz range.

To reveal the relationship between AE parameters and fracture mechanisms, several studies have been performed using different AE features, for instance, amplitude, energy, counts, etc. Furthermore, there are some researches that have used multi-parameter analysis to develop discrimination of AE events. Supervised pattern recognition based on the k-nearest algorithm was used for classification of damage modes in carbon fiber/epoxy composites by researchers. When the number of damage mechanisms is known, supervised pattern recognition is used, whereas unsupervised pattern recognition is performed without any previous knowledge. In the other study, unsupervised pattern recognition algorithm was used to analyse AE signals obtained from two SiCf/[Si-B-C] composites and could effectively discriminate between different matrix cracking types. Godin et al. used integration of k-means algorithm and Kohone's som for classification of AE signals and achieved attractive results. Also neural network method is accurate but suffers from large computational time. In addition, its performance depends on number of neurons and network structure.

Some other researchers used frequency domain for discrimination of AE signals. Discrete and continuous wavelet transform was used by Marec et al. to extract new time-scale descriptors to improve the characterization of fracture mechanisms. They used

fuzzy c-means clustering associated with a principal component analysis (PCA) to cluster the AE signals. It was found that the new descriptors are useful.

In this article, PCA was first employed to diminish the dimensionality of rather large data. The AE signals utilized for clustering analysis were obtained through the three-point bending test. After dimensional reduction, the datasets were clustered using integration of k-means and genetic algorithms. K-means algorithm is a powerful clustering algorithm, but its performance depends on the initial cluster centers. In order to solve this problem, GA was used as an efficient method to discover optimum cluster centers. In addition, in this study, wavelet packet transform (WPT) was used to study time-frequency domain. To analyse each domain of AE signals, energy criterion was used. Finally the achieved results were validated using microscopic observation by SEM.

Experimental Procedure

Materials and Specimen Manufacturing

The experimental work was carried out on the epoxy resin reinforced by the E-glass unidirectional and woven fiber with the density of 1.46 g/cm^3, 500 g/m^2 and 303 g/m^2, respectively. The laminates were provided by hand lay-up with compression molding. Rectangular plates of cross glass fiber/epoxy composite plates with blind holes in the center, were manufactured in the lab. Also, starter crack was created by inserting a Teflon film with a thickness of about 20 μm during the molding process as an initial crack for the delamination test (see Fig. 1). The specimen dimensions were 150 mm×50 mm×5 mm. For ease of working, the woven specimen is named S1 and the unidirectional specimen is named S2.

Testing Machine

A properly calibrated universal tensile test machine-Hiwa was used. Specimens were loaded in 0.2 mm/min and 2 mm/min. The load cell capacity of the test machine is 5000 N.

AE Device

The AE software AEWin and a data acquisition system, Physical Acoustics Corporation (PAC) PCI-2 with a maximum sampling rate of 40 MHz were used to record AE events. The AE sensor, called PICO, was a broadband, resonant-type, and single-crystal piezoelectric transducer from (PAC). The resonance frequency and the optimum operating range of the sensor were 513.28 kHz and 100-750 kHz, respectively. In order to provide good acoustic coupling between the specimen and the sensor, the surface of the sensor was covered with grease. The signal was detected by the sensor and enhanced by a 2/4/6-AST pre-amplifier. The gain selector of the preamplifier was set to 40 dB and test sampling rate was 1 MHz and 16 bits of resolution. This sampling rate selection is due to the fact that in composite materials, different failure mechanisms generate AE signals which have frequencies lower than 500 kHz. As shown in the Fig. 1, the specimens were placed in the testing machine and subjected to the compression loads through three point bending test. The applied compression loads versus displacement is stored digitally.

Clustering Techniques

Principal Component Analysis (PCA)

The PCA is a multivariate analysis device usually utilized to reduce dimensionality of a large dataset to permit a better vision and analysis of data. PCA was introduced in the previous works.

k-Means Algorithm

The object of k-means algorithm is to classify a set of n data points in m-dimensional space into k number of classes. The classification is done by minimizing the sum of squares of distances between data and the respective cluster centers. The first step of k-means algorithm is to partition the input data into k initial sets. After calculating mean point (centroid), a new partition is constructed by assigning each point to the cluster with nearest center. Then the new centroids are recalculated for the new clusters and the algorithm is repeated by alternate application of these two steps until the coordinates of cluster centers do not change any more. Since the number of classes is not known a priori, the algorithm must be executed for different values of k and the best partitioning must be defined by means of a validity criterion such as the Davis-Bouldin (DB) index. The DB index is calculated as follows:

$$DB = \frac{1}{k}\sum_{i=1}^{k}\max_{i\neq j}\left\{\frac{s_i + s_j}{d_{ij}}\right\} \qquad \text{(Eq1)}$$

Where s is the within-cluster distance, d the between clusters distance and k is the number of clusters. The low values of DB index indicate good clustering.

Algorithm of k-Means Genetic

The disadvantage of k-means algorithm is that its performance depends on the selection of the primary

cluster centers. In order to solve this trouble, GA was used as an efficient method to discover optimum cluster centers. Mixing the simplicity of k-means algorithm with the ability of GA, avoiding local optima, can give an optimum clustering of AE events.

The steps of this algorithm are explained bellow:

Step 1 Chromosome representation

Each chromosome is a series of real numbers representing the cluster centers.

Step 2 Population initialization

K random points are chosen from input dataset to form cluster centers.

Step 3 Clustering

In this step, each point x is assigned to the cluster with nearest center and then new centers are calculated by (Eq 2):

$$z_i^* = \frac{1}{n_i} \sum_{x_j \in C_i} x_j, \ i = 1, 2, ..., k \qquad \text{(Eq2)}$$

Where z_i^* is the new cluster center and ni is the number of points belonging to cluster Ci.

Step 4 Fitness computation

Fitness value is defined as the summation of the Euclidean distances of the points from their corresponding cluster centers (Eq 3):

$$Fitness\,value = \sum_{i=1}^{k} \sum_{x_j \in C_i} \| x_j - z_i \| \qquad \text{(Eq3)}$$

Where z_i denotes cluster center and k is the number of clusters. For optimum clustering, fitness value must be minimized.

Step 5 Selection

Two parents are selected from a population according to their fitness to create two new children. In this study, Roulette wheel selection with elitist selection was used. Elitist selection which copies at least one best solution without any changes to a new population, guaranties the best solution ever found to survive to end.

Step 6 Crossover

In this step, two parents exchange their information to create new children with a specified crossover probability.

Step 7 Mutation

After crossover is performed, mutation takes place according to the (Eq 4):

$$r' = \begin{cases} r \times (1 \pm 2\Delta) & if\ r \neq 0 \\ (\pm 2\Delta) & if\ r = 0 \end{cases} \qquad \text{(Eq4)}$$

Where r is the value at a gene position before mutation, r′ after mutation and Δ is a number in the range (0,1) generated with uniform distribution. The (+) or (-) sign both have same probability to occur.

Step 8 Checking stopping criterion

The algorithm should be repeated while the stopping criterion is reached. In this paper, maximum number of iterations was used as stopping criterion.

A brief description of fracture characterization procedure is shown in Fig. 2.

Table 1 summarizes the initial parameters of KGA. Also, the flowchart of the algorithm is shown in Fig. 3.

Wavelet-based Methodology

Wavelet transform (WT) is a powerful signal-processing tool introduced in the mid-1980s. WT has been used successfully by various researchers for analysing AE signals.

Wavelet is a waveform of effectively limited duration with zero average value. In this study, for the analysis of waveforms, discrete wavelet transform (DWT) and wavelet packet transform (WPT) were used. DWT splits a signal into approximations and details. The approximations are the high-scale, low-frequency components, and the details are the low-scale, high-frequency ones. In some special applications, where the important information is located in higher frequencies, the decomposition process of only the approximation components at each level is not sufficient. Hence, in order to improve the time-frequency analysis, further decomposition of detail components to its own detail and of approximation components is necessary.

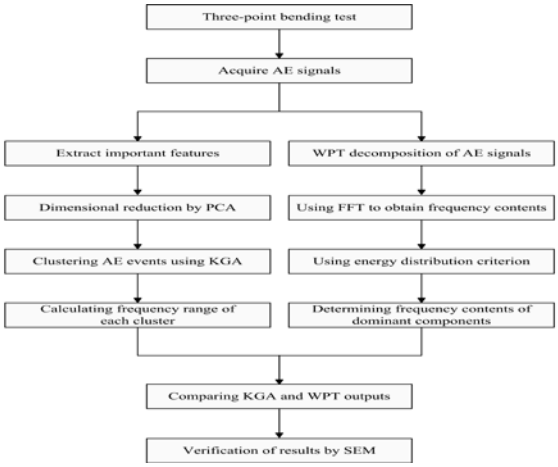

FIG. 2 SUCCINCT EXPLANATION OF PROCEDURE OF DAMAGE CHARACTERIZATION

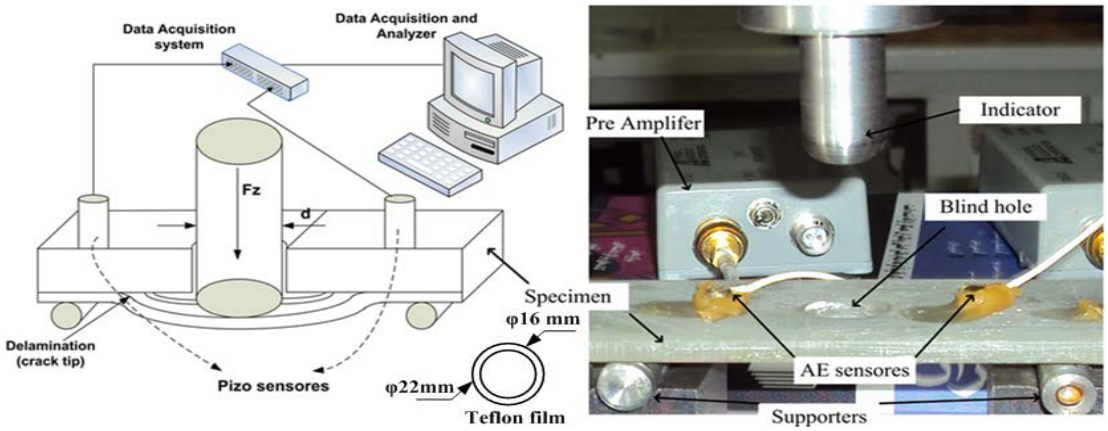

FIG.1 THREE POINT TEST AND AE DEVICE SETUP

This is called WPT which offers the richest analysis. Fig. 4 shows the WPT tree for a signal.

In this article, the energy criterion was employed to find the dominant components related to different damage modes. If $f_1^j \ldots f_i^j$ denote the components of jth level of the decomposed signal, the component energy at level j can be calculated from (Eq 5):

$$E_j^i(t) = \sum_{\tau=t_0}^{t} (f_j^i(\tau))^2 \qquad \text{(Eq5)}$$

Then the total energy of signal is defined by (Eq 6):

$$E_{Total}(t) = \sum_j E_j^i(t) \qquad \text{(Eq6)}$$

In order to find energy distribution displayed at different components, the ratio of energies at different levels to the total energy must be calculated. Equation 7 determines a relative energy distribution at each level:

$$p(t) = \frac{E_j^i(t)}{E_{Total}(t)}, \; i = 1....2^j \qquad \text{(Eq7)}$$

Results and Discussion

During quasi-static 3-point bending tests, different mechanisms control the fracture mechanics process. Hence, different regions on AE counts plot can be differentiated (see Fig. 5).

Region 1: When there is no considerable damage in the specimen. In this region, no crack activity is observed and the damage level is negligible.

Region 2: Some strong AE peaks become detectable, when the load reaches a specific level. These relatively high energy signals are associated with the initiation and propagation of delamination.

Region 3: This region in AE-displacement plot is related to the propagation of delamination that causes absolute fracture.

Typical raw waveform of AE signals in these regions is shown in Fig. 6. In the analysis of fracture mechanisms these events play significant roles in the analysis of fracture mechanisms.

During the quasi-static three-point bending test of the specimens, S1 and S2, about 6000 and 10000 AE waveforms were detected. Six important AE features peak amplitude, rise time, count, duration, energy, and average frequency were extracted using the threshold value of 40 dB. In order to reduce the dimensionality of rather large dataset and better visualization of the data in a two-dimensional subspace, PCA was utilized. Since the variables were not in same units, they were first standardized by their standard deviations.

The cumulative sum of the variances of the two first PCS was about 86% of the total variance of the input data for S1, and 89% for S2. In this article, two first PCS were kept for clustering analysis. After dimensional reduction, the AE events were clustered applying KGA.

TABLE 1 INITIAL PARAMETERS OF KGA

Initial population	Crossover rate	Mutation rate	Maximum number of interaction
100	0.7	0.01	500

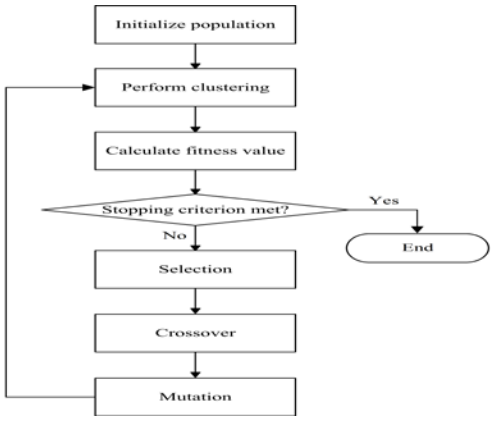

FIG. 3 FLOWCHART OF KGA

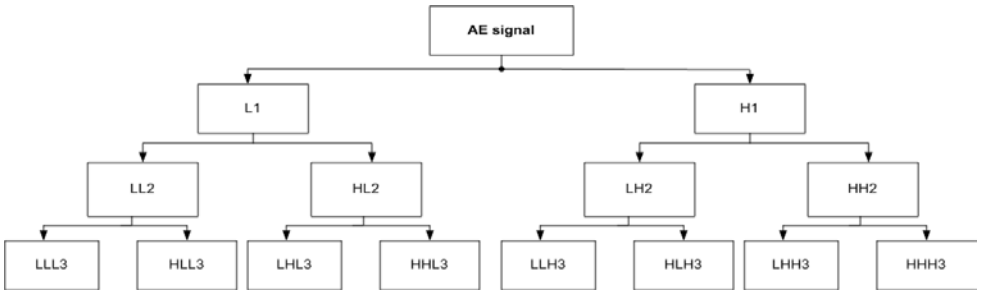

FIG. 4 PACKET WAVELET TRANSFORM TREE

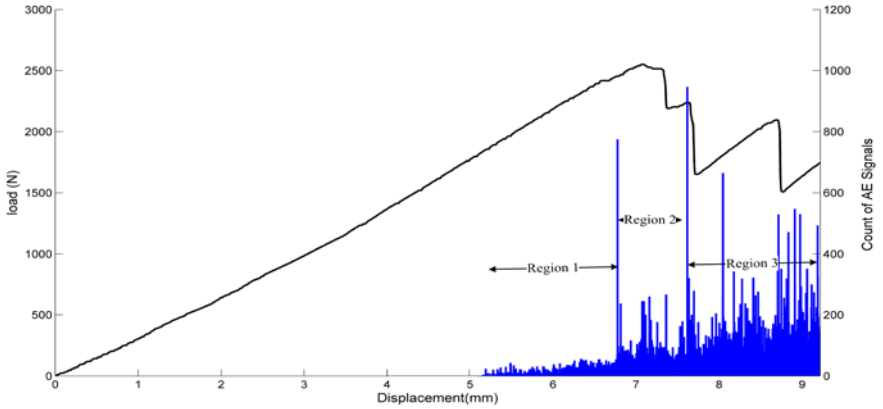

FIG.5 DIFFERENT REGIONS ON AE COUNT PLOT DETERMINE FRACTURE MECHANISMS FOR S2

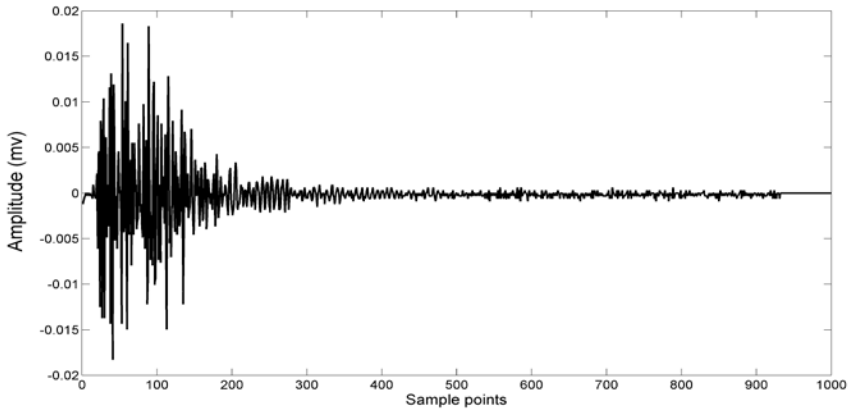

FIG.6 TYPICAL AE WAVEFORM

The optimum number of clusters was determined applying Davis-Bouldin validity (DB) index. For this purpose, the KGA was executed with values of k from 2 to 10 and the DB index was calculated for each run. It should be noted that in this article, the signals obtained from S1 and S2 are analysed using introduced methods, but the results related to S1 were depicted and the results of S2 were just reported in the text. Figures are related to the results of S1. Average DB index versus the number of clusters (k) is shown in Fig. 7. The achieved results show that the optimum number of clusters which minimizes the DB index is three. PCA visualizations of KGA clustering for S1 is shown in Fig. 8. Distribution of AE events in various clusters is summarized in Table 2. The results show that AE signals are well separated during the first principal direction. For S1 and S2 the first and the second clusters contain 94% and 84% of entire AE signals, respectively.

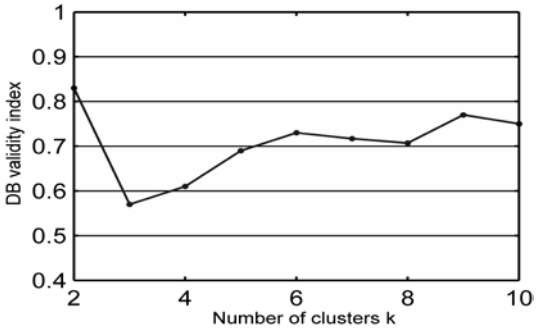

FIG. 7 DB INDEX VERSUS NUMBER OF CLUSTERS FOR S1

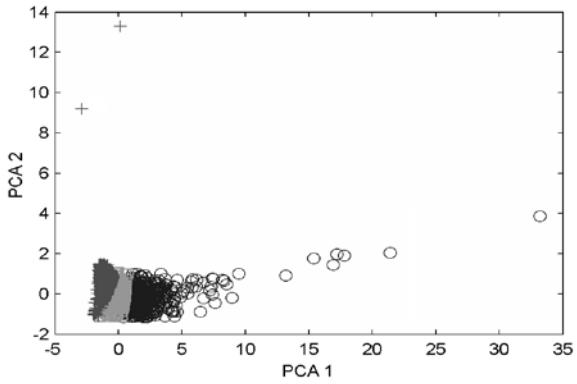

FIG.8 PCA VISUALIZATION OF KGA CLUSTERING FOR S1

TABLE 2 DISTRIBUTION OF AE SIGNALS IN THREE CLUSTERS

Specimen	First cluster, %	Second cluster, %	Third cluster, %
S1	64	30	6
S2	16	27	57

Among various AE parameters, frequency was best distinguished. Therefore, for damage characterization, frequency was applied as a capable AE descriptor. The frequency distribution charts for S1 is shown in fig. 9. Dominant frequency ranges of the achieved clusters are illustrated in Table 3. In each cluster, there are several frequencies with low densities that should be related to some other events. Also there are some overlaps in the results. These overlaps could be due to some other unknown damage mechanisms which may cause events with different frequency ranges. Recognition of these events was not studied in this article, because they involve very small portions of AE signals.

The frequency ranges achieved by KGA were then compared with WPT results. For WPT analysis, AE events were decomposed into three wavelet components using debauchees D10. In order to ensure that certain decomposition is adequate or more levels are needed, the mathematical criteria called entropy criteria are applied. Fig. 10 shows the three-level WPT decomposition of an AE event for S1. Fig. 11 shows that each component represents a specific frequency range which can be achieved applying FFT method.

In order to discriminate fracture mechanisms, energy criterion was applied. The energy proportion of each component of level three was compared with the total energy of the AE events based on the (Eq 5-7). Fig. 12 shows energy distribution of level three components for S1.

The greatest proportion of energy is concentrated in the components LHL3, LLH3, LHH3. For S1, the most dominant components are LHL3 and LLH3, while for S2, the most important ones are LLH3 and LHH3 from energy point of view. The energy distribution pattern at the same component is dissimilar for various specimens. Reason for this dissimilarity is various main fracture mechanisms for each specimen. The frequency range of dominant components was summarized in Table 4.

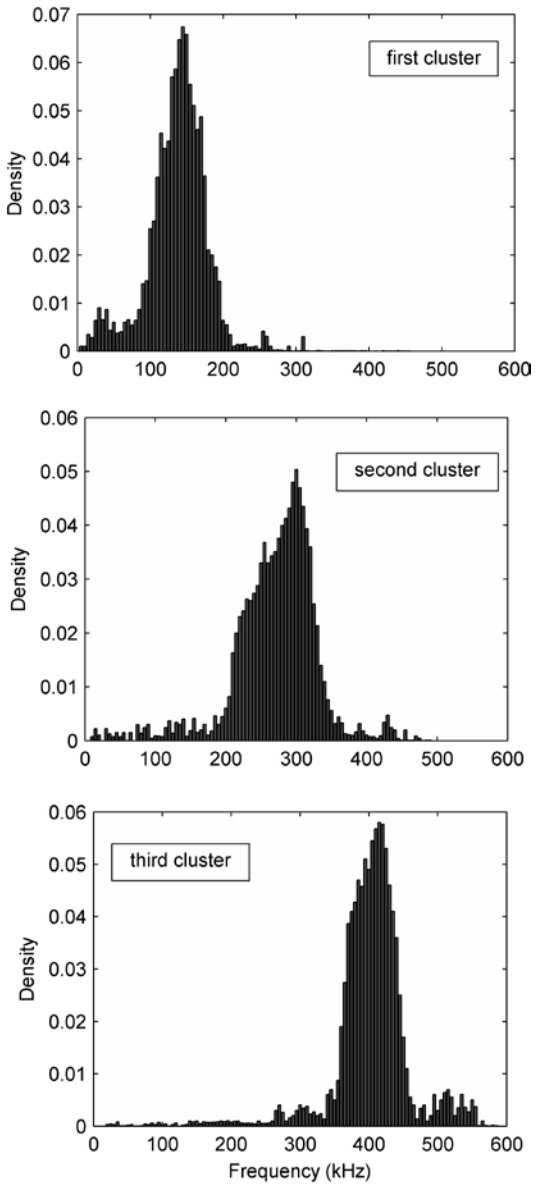

FIG. 9 FREQUENCY DISTRIBUTION CHART FOR S1

TABLE 3 FREQUENCY RANGE OF THE OBTAINED CLUSTERS

	Frequency range, kHz		
Specimen	First class	Second class	Third class
S1	90-195	210-335	360-450
S2	85-180	205-325	345-445

TABLE 4 FREQUENCY RANGE OF DOMINANT COMPONENTS

Component	LHL3	LLH3	LHH3
Frequency range, kHz	100-190	200-320	355-450

The prior studies in this field indicated that there are three prevalent fracture mechanisms for fiber-reinforced composite materials: fiber-matrix debonding, matrix cracking, and fiber breakage. SEM observation taken in the near of starter crack shows these fracture mechanisms. For S1, fiber-matrix debonding and matrix cracking are the most dominant fracture modes shown in Fig. 13. A little fiber breakage was also detected. For S2, debonding and fiber breakage are the most important damage modes. Fiber-bridging phenomenon in unidirectional composites is the main reason for fiber breakage in S2.

The frequency contents of glass-epoxy debonding are between frequency contents of fiber breakage and matrix cracking. Therefore, the AE events of the first cluster are representative of matrix cracking, while the AE signals of the second and the third clusters are associated with fiber-matrix debonding and fiber breakage, respectively.

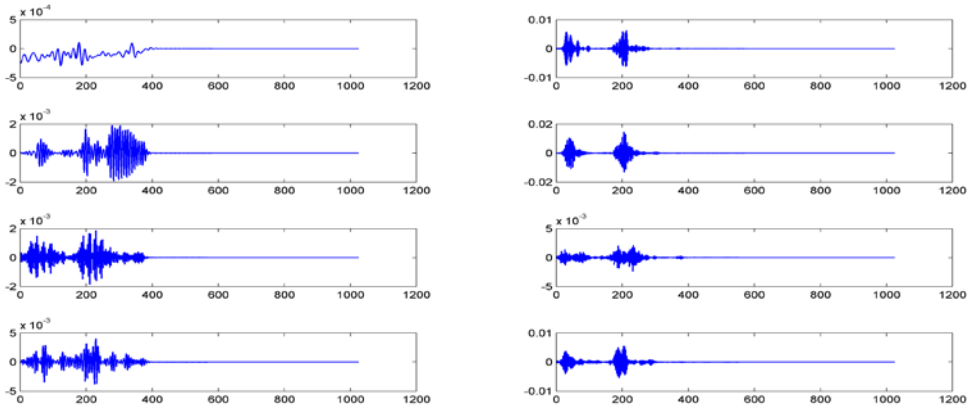

FIG. 10 THREE-LEVEL WAVELET PACKET DECOMPOSITION OF AN AE SIGNAL FOR SPECIMEN S1

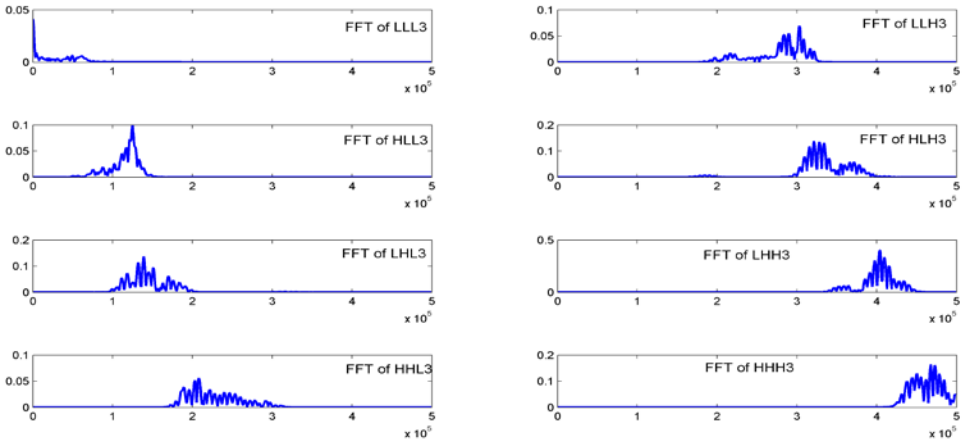

FIG. 11 LEVEL 3 FFT OF THE DECOMPOSED COMPONENTS

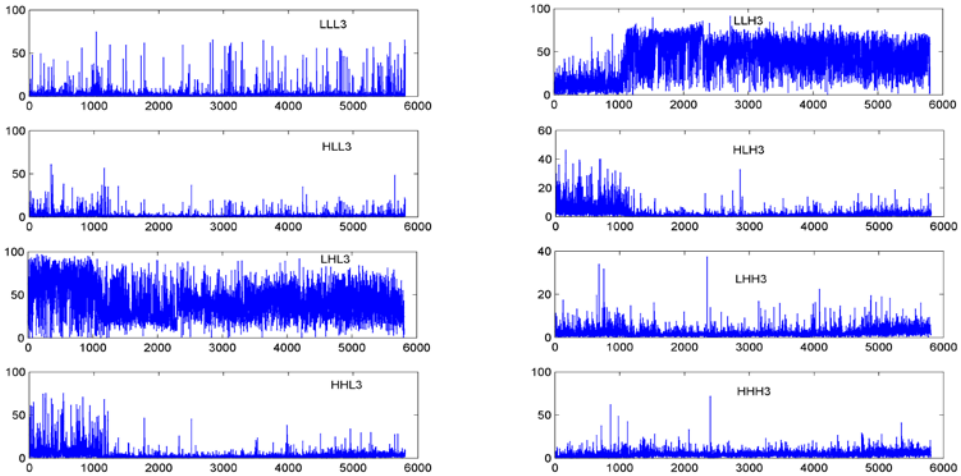

FIG. 12 ENERGY PERCENTAGE OF EACH COMPONENT OF LEVEL 3 FOR S1

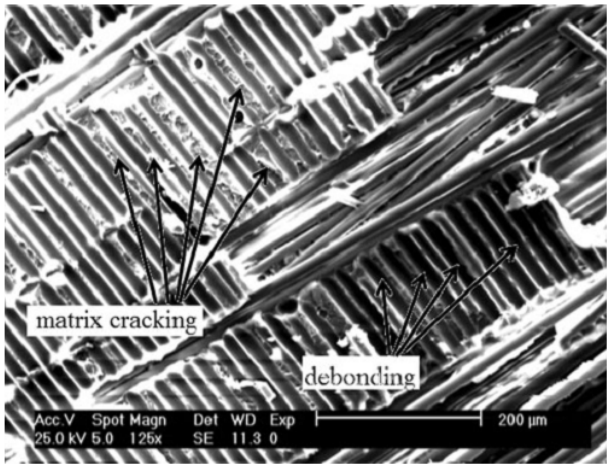

FIG. 13 SEM OBSERVATION OF DOMINANT FAILURE MECHANISMS FOR S1

Conclusion

In this work, after investigating the quasi-static three-point bending test by AE method, it is desirable to discriminate various fracture mechanisms of glass/epoxy composites. Wavelet packet techniques (WPT) and integration of genetic and k-means algorithms (KGA) were used for the processing of the AE waveforms obtained during the test. SEM observations showed that the dominant failure modes such as fiber breakage, debonding, and matrix cracking were the sources of AE signals. But the objective of this study was to determine which frequency range corresponds with these failure modes. For this investigation KGA and WPT were used, and then the outputs of these two techniques were compared with each other. Based on the WPT results, it was found that there are three dominant class centers with frequency ranges at 100-190, 200-320 and 355-450 kHz. Using KGA analysis, three dominant frequency ranges were found and the frequency ranges obtained by WPT were in good consistency with KGA outputs. Each frequency range was related to a distinct fracture mode. This correlation was due to the different visco-elastic relaxation processes which generate specific frequency range due to different failure mechanisms. It was found that the AE events of the first frequency range were related to matrix cracking and the second and third were related to fiber-matrix debonding and fiber breakage, respectively. According to the distribution of AE events in various clusters, debonding and matrix cracking were the most important fracture mechanisms for S1, while fiber breakage and debonding were the most dominant fracture mechanisms for the S2. It was concluded that WPT is a powerful method to analyze AE signals in frequency domain. Also, KGA distinguished different damage mechanisms from AE signals, in a more precision and low time compared to other methods.

ACKNOWLEDGMENT

The authors would like to thank the Department of Mechanical Engineering at Amirkabir University of Technology for providing the facilities for this study.

REFERENCES

Ativitavas, Nat and Pothisiri, Thanyawat et al. “Acoustic emission characteristics of pultruded fiber reinforced plastics under uniaxial tensile stress.” Proceedings of European WG on AE, Berlin, 447-454, 2004.

Bandyopadhyay, Sanghamitra and Maulik, Ujjwal“An evolutionary technique based on K-Means algorithm for optimal clustering in RN.” Inf. Sci. 146 (2002): 221-237.

Barré, Sébastien and Benzeggagh, Malk. “On the use of acoustic emission to investigate damage mechanisms in glass-fibre-reinforced poly-propylene.” Compos. Sci. Technol 52 (1994): 369-376.

Bouldin, Donald W. and Davies, David L. “A cluster separation measure.” IEEE Trans. Pattern Anal. Mach. Intell 1 (1979): 224-227.

Chen, Wen-Chou. “Some Experimental Investigations in the Drilling of Carbon Fiber-reinforced Plastic (CFRP) Composite Laminates. ” Int. J. Mach. Tools Manuf 37 (1997): 1097–1108.

Chowdhury, Nirmalya and Murthy, ChivuKula A. “In search of optimal clustering using genetic algorithms.” Pattern Recognit. Lett. 17 (1996): 825-832.

Godin, Nathalie and Moevus, Mariette et al. “Analysis of damage mechanisms and associated acoustic emission in two SiCf/[Si–B–C] composites exhibiting different tensile behaviours.” Part II: Unsupervised acoustic emission data clustering, Compos. Sci. Technol. 68 (2008): 1258–1265.

Godin, Nathalie et al. “Integration of the Kohonen’s self-organizing map and k-means algorithm for the segmentation of the AE data collected during tensile tests on cross-ply composites.” NDT&E Int. 38 (2005): 299-309.

Grossmann, Alexander and Morlet, Jean “Decomposition of hardy functions into square integrable wavelets of compact shape.” SIAM J. Math. Anal. 15 (1984): 723–736.

Haykin, Simon. Neural Networks-A Comprehensive Foundation, 2nd ed., New York: Macmillan College, 1994.

Jolliffe, Ian T. Principal Component Analysis, 2nd ed, springer series in statistics, 2002. Actuat B-Chem, 81, 2002, 313 – 315.

Kostopoulos, Vassilis et al. "On the identification of the failure mechanisms in oxide/oxide composites using acoustic emission." NDT&E Int. 36 (2003): 571-580.

Likas, Aristidis and Vlassis, Nikos et al. "The global k-means clustering algorithm, Pattern Recognit." 366 (2003): 451-461.

Marec, Anne et al. "Damage characterization of polymer-based composite materials: Multivariable analysis and wavelet transform for clustering acoustic emission data." Mech. Syst. Signal Process 22 (2008): 1441-1464.

Morscher, Gregory N. et al. "Determination of interfacial properties using a single-fiber microcomposite test." J. Am. Ceram. Soc. 79 (1996): 1083–91.

Murthy, Crl and Ravishankar, Sri. "Application of acoustic emission in drilling of composite laminates. " NDT&E Int. 33 (2000): 429-435.

Ohtsu, Masayasu and Ono, Kanji. "pattern recognition of acoustic emission signals from carbon fiber/epoxy composites." 7th international acoustic emission symposium, Zao, Japan, 1987.

Pappas, Y.Z et al. "Failure mechanisms analysis of 2D carbon/carbon using acoustic emission monitoring." NDT&E Int. 31 (1998): 157-163.

Qi, Gang. "Wavelet-based AE characterization of composite materials." NDT&E Int. 33 (2000): 133-144.

Yamaguchi, Kusuo et al. "Acoustic Emission technology using multi-parameter analysis of waveform and application to GFRP tensile tests.", Acoustic Emission, current practice and future directions, ASTM STP 1077, 123-143, Philadelphia, PA , 1991.

International Journal of Material Science (IJMSCI) Volume 4 Issue 1, March 2014 www.ij-ms.org
doi: 10.14355/ijmsci.2014.0401.05

Development of One-hour Fire-resistive Building Materials Made of Combustible Japanese Cedar Using Laser Incising

Keisuke Ando[*1], Nobuaki Hattori[**1], Toshiro Harada[2], Daisuke Kamikawa[2], Masayuki Miyabayashi[3], Kouta Nishimura[4], Norichika Kakae[4], Keiichi Miyamoto[4]

[1]Graduate School of Agriculture, Tokyo University of Agriculture and Technology
3-5-8, Saiwai-cho, Fuchu-shi, Tokyo, Japan

[2]Forestry and Forest Products Research Institute

[3]T.E. Consulting Inc.

[4]Kajima Technical Research Institute

[*]andok@cc.tuat.ac.jp; [**] hattori@cc.tuat.ac.jp

Abstract

Conventional glued-laminated timber (glulam) was not permitted any more to be applied to a wooden building in the fire preventive district since the amendments of the Building Standard Law in 2000. The Japanese Government set the self-sufficiency rate of the domestic wood supply at 50% within ten years in 2011 and enacted the new legislation to promote wooden structures and wooden interior decorations in public buildings as long as possible. Therefore, it is strongly desired to develop fireproof structural materials usable in urban area to achieve goals.

Therefore, one-hour fireproof glued-laminated timber (glulam) and cross laminated timber (CLT) were developed made of Japanese cedar (*Cryptomeria japonica* D. Don) which is the major species in Japan and combustible by incision to fire-die-out part of lamina with CO_2 laser. The structure in cross-section of the glulam consists of three zones, namely, load-bearing part (untreated glulam), fire-die-out part impregnated fire-retardant chemicals and surface part (untreated lamina). An one-hour fire-resistive CLT was also developed using the same concept as the glulam and its performance was confirmed by the fire-resistance test. The first wooden building whose main structural members were made of the fireproof glulam marketed as FR wood® was also introduced briefly.

Keywords

Laser Incising; Fireproof; Japanese Cedar; Glulam; Construction

Introduction

A building of three stories or more must be a fireproof building in the fire protection districts in Japan by the Building Standard Law revised in 2000 after the Great Hanshin-Awaji Earthquake. Therefore, buildings in this area have to be constructed with fireproof structural members designated as more than one-hour resistance for fire by the Ministry of Land, Infrastructure, Transport and Tourism. However, it is very hard for structural members to be certified as one-hour resistant because of very severe fire-resistance test, even if the material is steel.

The Japanese Government set the self-sufficiency rate of the domestic wood supply at 50% within ten years in 2011 and enacted the new legislation to promote wooden structures and wooden interior decorations in public buildings as long as possible.

Therefore, it is strongly desired to develop fireproof wood members usable in urban area to achieve goal. So, several types of one-hour fireproof structural members made of wood have been developed mainly by major construction companies. But, most of them were made of not only lumber but also other materials such as steel, mortar or gypsum board. It may be difficult for us to call them as wooden construction.

Laser incising was judged to be most likely pretreatment to impregnate fire-retardant chemicals promptly according to the research experience of Hattori's laboratory during development of the laser technology about incising more than two decades. Therefore, we decided to develop an one-hour fireproof glued-laminated timber (glulam) and cross laminated timber (CLT) made of only sugi (Japanese cedar) which can be called as wood construction. The key to success was impregnation of fire-retardant chemicals uniformly across the required part of sugi lamina which burns easily using the help of laser incising as a pretreatment and commercially available

fire-retardant chemicals.

Materials and Methods

Materials

Lamina used in a series of experiments is sugi (*Cryptomeria japonica* D. Don,).

To develop one-hour fireproof glulam and CLT, fire-retardant chemicals called carbamyl polyphosphate were impregnated into fire-die-out part of laser incised lamina by conventional pressure process defined by JIS A 9002 with minimum variation in net retention.

Methods

The laser used in this paper is slab type CO_2 laser (DC 025, Rofin-Baasel Japan Co.).

A laser incising system was developed by our laboratory as shown in Fig. 1 using commercially available slab CO_2 laser and the processing head designed for this purpose. The characteristics of the system is the adoption of long focus lens such as 20 inches made of single-crystalline ZnSe.

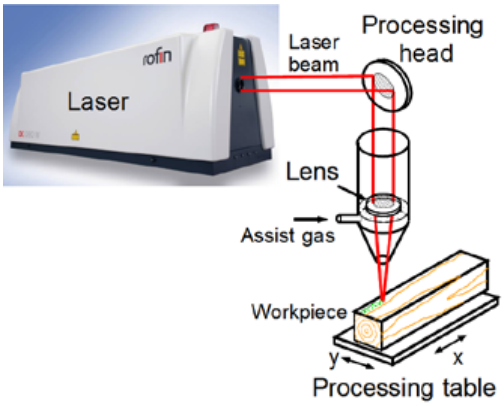

FIG. 1 LASER PROCESSING MACHINE FOR INCISING WITH SLAB CO_2 LASER.

Laser incising was done to the fire-die-out part of a lamina with density of 1600 holes/m^2 whose diameter is up to 1.5 mm as shown in Fig. 2. Fire-retardant chemicals were then impregnated into incised laminae properly. Lamina was stacked and glued for fireproof glulam and CLT.

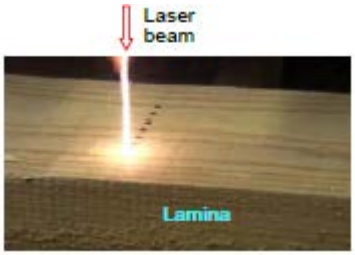

FIG. 2 LASER INCISING TO SUGI LAMINA WITH SLAB CO_2 LASER.

Results and Discussion

Laser Incising

Shapes of cross-section of pinholes by laser were shown in soft X-ray photo of Fig. 3 with those of drill.

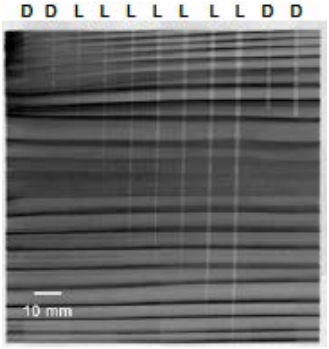

FIG. 3 SOFT X-RAY IMAGE OF SUGI LAMINA HOLED BY LASER WITH THOSE OF DRILL IN SUGI LAMINA BY.
(Holes by drill of ø1.0, 1.5 mm, by laser of 25, 50, 100, 150, 200, 300, 400 msec in pulse duration with 1 kW power, and by drill of ø2.0, 2.5 mm, respectively from left.)

It is said that shape of a hole by laser is almost conical and aspect ratio of the hole is considerably high compared to those of drill incising.

Development of Fire-resistive Members

The basic structure developed for fire-resistive members is shown in Fig. 4. The structure consists of load-bearing part (Untreated glulam), fire-die-out part (Impregnated with fire-retardant chemicals for 60 mm in width) and surface part (Untreated lamina 10 mm in thickness). The surface part covers the fire-die-out part to prevent efflorescence when fire-retardant chemicals immersed as white crystals by moisture fluctuation in lumber. This structure can be also applicable to CLT and other fire-resistive members.

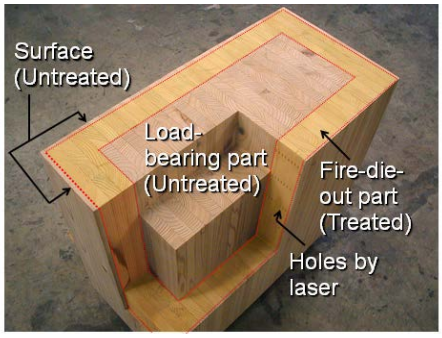

FIG. 4 STRUCTURE OF FIRE-PROOF GLULAM DEVELOPED.

The retention of fire-retardant chemicals in the laser-incised area was 150 ~ 200 kg/m^3 as solid content. There was big difference in retention of sugi lamina with and without incising and little difference between laser and drill incising. When a lamina with knots is used, it may be better to increase the incising density.

The fire-resistance tests of sugi glulam with different sizes of cross section have been conducted at a recognized testing center. The maximum and minimum cross sections were 350 x 700 mm and 240 x 240 mm whose length was the same as 3300 mm. They were heated for one-hour under the predefined load suitable for size of column and beam, respectively according to the heating schedule by ISO 834-1 until all fire died down as shown in Fig. 5.

Before heating During heating After heating

FIG. 5 FIRE TEST OF GLULAM.

One of the results of temperature course during the fire-resistance test of 350 x 700 mm was shown in Fig. 6. It is clear that the maximum temperature at the boundary of fire-die-out part and load-bearing part never goes over 260℃ that is the threshold temperature of char.

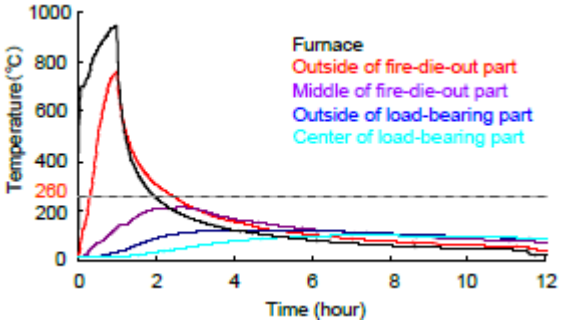

FIG. 6 TEMPERATURE COURSE IN GLULAM OF 350 X 700 MM DURING FIRE-RESISTANCE TEST.

This specimen could be judged to stop burning spontaneously and thus being one-hour fireproof glulam. If the fire-die-out part was thickened somewhat, two-hour fire-resistive performance can be realized according to the preliminary fire-resistance test.

Based on a series of fire-resistance test results, Kajima Corporation got for the first time a certificate of one-hour fireproof sugi glulam from Ministry of Land, Infrastructure, Transport and Tourism and named it FR wood®. The first building whose main column and beam were composed of FR wood® was completed in fire protection district of downtown Tokyo in May 2013 as shown in Fig. 7 and started to use as a café. The size of FR wood® is 260 x 290 mm for three independent columns and two flying beams.

Three storied Café using FR wood® built in May 2013
Building area: 132 m², Floor area: 243 m²,
Client·basic design: Otoha bldg., Design: Kajima Design Corp., Interior ·FFE: ILYA, Builder: Sumitomo Forestry Co., Ltd., Sakamoto bldg.

FIG. 7 STRUCTURE OF FIRE-PROOF GLULAM DEVELOPED.

We also developed CLT with fire-die-out layer of 50 mm and implemented the fire-resistance test. Though the surface lamina burned in an early stage of the fire-resistance test, fire died out before burnout of surface layer. It is clear that the maximum temperature at the boundary of fire-die-out layer and center one is 133℃ and never goes over 260℃ as shown in Fig. 8. There was no difference caused by the direction of laser incising to lamina for fire-die-out. As the char depth was 29 ~ 41 mm (average: 35 mm) and the maximum plane displacement was 4.4 mm, this specimen could be judged to stop burning spontaneously and thus one-hour fireproof CLT.

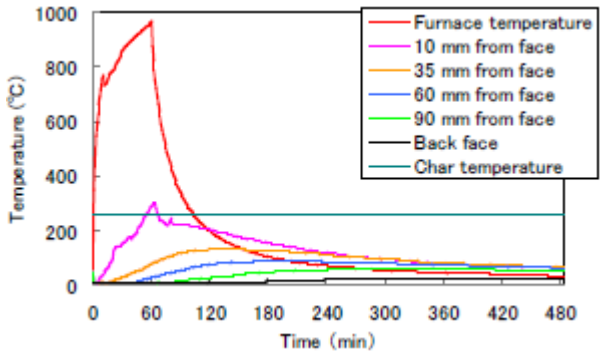

FIG. 8 TEMPERATURE COURSE IN CLT DURING FIRE TEST [6].

The next tasks will be to reduce costs of one-hour members by decreasing incising density and concentration of fire-retardant chemicals and to develop two-hour fireproof wooden structural members.

Conclusions

Development of laser incising has been made vigorously for the past two decades and could be reached to practical use this year. In the meanwhile, two types of high power CO_2 lasers have been used and suggested us the importance of laser performance to incise lumber from various view points such as cracks in wood, passage from a hole, aspect ratio of a pinhole and retention of fire-retardant chemicals with even penetration comparing to other mechanical incising methods. These advanced performances of laser incising could enable us to develop a one-hour fireproof structural member named FR wood® at last.

Laser processing may have potentialities in wood processing, though this technology is minor in wood research and industry unlike the fields of engineering. This is because of relatively high initial cost, the necessity of laser technology and the experience of laser operation. Therefore, the performance of drill incising shall be examined promptly too.

ACKNOWLEDGMENT

This work was partially supported by a Grant-in-Aid for Scientific Research (A) (No. 22248019) from Japan Society for the Promotion of Science.

REFERENCES

Daisuke KAMIKAWA, Toshiro HARADA, Masayuki MIYABAYASHI, Norichika KAKAE, Kouta NISHIMURA, Keiichi MIYAMOTO, Tomio OHUCHI, Keisuke ANDO and Nobuaki HATTORI: DEVEROPMENT OF FIREPROOF GLUED LAMINATED LUMBERS WITH FIER-RETARDANT LAMINE - One and Two hour loaded fire resistance tests on Japanese cedar laminated lumber columns-, Transactions of Architectural Institute of Japan, J. Environmental Engineering, **75** (657), 929-935 (2010)

Kajima Co., and Sumitomo Forestry Co., Ltd.: Brochure of oto no ha Café, May 22, pp.14 (2013)

MORITA Miyabi, ANDO Keisuke, HATTORI Nobuaki, KAMIKAWA Daisuke, HARADA Toshiro, MIYABAYASHI Masayuki, KAKAE Norichika, NISHIMURA Kouta, MIYAMOTO Keiichi: Fire-resistance Test of Sugi Cross Laminated Timber made of laser incised lamina impregnated with fire-retardant chemicals, Proceedings of 62nd Annual Meeting of Japan Wood Research Society, Hokkaido University, Sapporo, March 15, No. H15-P-AM19, 145 (2012)

Nobuaki HATTORI, Keisuke ANDO, Toshiro HARDA, Masayuki MIYABAYASHI, Masao SHIOZAKI: Fireproof glued laminated timber, Patent No. 4958098, March 30, 2012

Norihiko YAMANE: Laser Incising of Wood-Hole shapes by different types and methods of laser and preservative impregnation to incised lumber--, Master thesis, Graduate School of Agriculture, Tokyo Univerisity of Agriculture and Technology, pp.152 (1992)

Toshiro HARADA, Keisuke ANDO, Masayuki MIYABAYASHI, Tomio OHUCHI, Keiichi MIYAMOTO, Daisuke KAMIKAWA, Nobuaki HATTORI: Flame Die-out of Glued Laminated Japanese Larch Lumber Columns with a Fire-retardant Shell-layer, Mokuzai Gakkaishi, **54** (3), 139-146 (2008)

Yue Wang, Keisuke Ando, Nobuaki Hattori: Changes in the anatomy of surface and liquid uptake of wood after laser incising, Wood Science and Technology, **47** (3), 447-455 (2013)

International Journal of Material Science (IJMSCI) Volume 4 Issue 1, March 2014 www.ij-ms.org
doi: 10.14355/ijmsci.2014.0401.06

Effect of Modified Polyorganosiloxane on Physical Properties of Acrylate Hard Coating

Seung Woo Bak[1], Doo Whan Kang[2], Ho-Jong Kang[*3]

[1,2,3]Department of Polymer Science and Engineering and Center for Photofunctional Energy Materials
Dankook University, Gyeonggido, Korea, 448-701

[1]tmddn0723@hanmail.net; [2]kdoowh@dankook.ac.kr; [*3]hjkang@dankook.ac.kr

Abstract

Rubber toughened acrylate was investigated as a protective hard coating material for plastic film to improve the flexibility while maintaining intrinsic hardness of acrylate. Polyorganosiloxane(POS) was chosen as a rubber phase to apply thin acrylate coating. Poly(methyl-vinyl) siloxane (PMVS) and modified polydimethylsiloxan (PDMS) having urethane and urea linkage were synthesized and also introduced as a rubber toughening phase. Increasing PMVS content in acrylate caused the increase of flexibility as well as hardness. However, the printability was dramatically dropped due to the increase of hydrophilicity on the coating surface by PMVS. Modified PDMSs having urethane and urea linkage in main chain enhanced the flexibility and hardness similar to PMVS while maintaining hydrophobicity which affected the printability in the coating surface. In addition, it was found that PMVS and modified PDMSs did not affect the optical transmittance in acrylate coating.

Keywords

Hard Coating; Acrylate; Polyorganosiloxane; Rubber Toughening; Flexibility; Hardness; Printability

Introduction

Optical plastic films often require the under or top thin coating to satisfy the various functional demands for electronics (Holman, 1991). The protective film is one of important optical film since the mobile electric displays have been developed rapidly and they need to prevent various damages from severe environmental exposure. Recently, the flexible display was introduced to the display market and the flexibility of protective film became important issue along with maintaining of hardness required for protective film.

In general, the protective film is made by acrylic based coating material since it has superior physical properties (Kuraoka, 2005) such as wear resistance (Ryntz, 2000), hardness and optical properties (Takaki, 1988). However, the intrinsic rigidity of acrylate caused the crack formation when the bending was applied to the thin acrylate coated optical film. Many studies for the development of flexible coating materials have been carried out to overcome this disadvantage (Schwalm, 1997). It was well known that the crack formation characteristic depended upon the degree of crosslinking in acrylic compound during the UV curing in coating material. In order to control the degree of crosslinking, UV curing mechanism should be understood in coating materials which consists of acrylic oligomer, acrylic monomer, solvent, photo initiator and various additives(Tanglumeler, 2006). It was well expected that lowering of crosslinking density might improve the flexibility while hardness for protecting the scratching might grow down. Rubber toughening in rigid polymeric material has been widely used in polymer industry to reduce the rigidity of hard plastic material. This concept may be applied to coating industry as well. Silicone compound has been introduced as a rubber toughening phase to acrylate since it has high transparency in visible light and ultraviolet light. Especially, Si-O bond of silicone compound has very low rotation energy compared to C-C bond(Kim, 2001). It is free in rotation thus having flexibility in broad temperature ranges.

In this study, various polyorganosiloxanes were mixed with acrylate to improve the flexibility in the acrylate coated PET film. PMVS was ring-opening polymerized using 1,3,5-trimethyl-1,3,5-trivinyl cyclosiloxane and modified PDMSs were synthesized through the urethane and urea reaction and these were applied to acrylate coating. The effects of PMVS and modified PDMSs on physical properties of coated PET film such as flexibility, hardness, surface characteristics and optical transmittance were investigated.

Experimental

Materials

Polymethylvinylsiloxane(PMVS) and modified PDMSs were synthesized based on our previous studies(Kang,

2012; Kang, 2013). PMVS and modified PDMSs were mixed with dipentaerythritol hexa acrylate(Miramer M610; Miwon, M_w: 524 g/mol) with 1-hydroxy-cyclohexyl-phenyl-ketone(Irgacure 184; Ciba) as a photo initiator. The POS content in acrylate was in the range of 3 – 21 wt. % and applied photo initiator was 0.66 wt. %. MEK (Duksan) was used as coating solvent and the solid content in coating solution is 50 wt. %. Fig. 1 shows the chemical structures of PVMS, PDMSs, and acrylate used in this study.

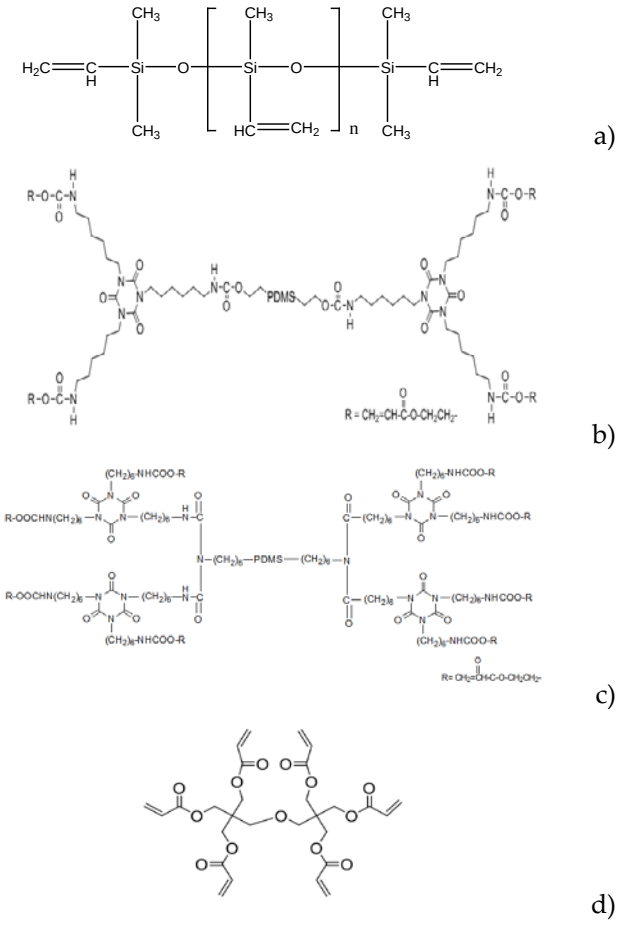

FIG. 1 THE CHEMICAL STRUCTURES OF A) PVMS, B)URE-THANE MODIFIED PDMS, C) UREA MODIFIED PDMS AND D) ACRYLATE

Preparation of Coated Films

PET film (Toyobo A4300; thickness:188 μm) was used as a substrate and coating was performed by wire bar (No. 05) and dried at 80°C for 60 sec. The ultraviolet curing was carried out for 30 sec (270 mW/cm²) using Cure Zone 2 (Daeho Glutech Co.) with high pressure mercury lamp. The thickness of acrylate coating on PET film was found to be 5-6 μm.

Characterizations

Scratching test was carried out by the pencil hardness tester equipped with heat-treat steel rod having 60° shaved end tip under 50 g of weight. Depth of scratching was measured by surface profiler (Dektak 150, Vecco). Bendability test was done to measure the flexibility of coated film. Film was rolled up 5 times repeatedly on the metal rod having 7-16 mm external diameter and then checked whether crack was formed or not on the coated surface. Flexibility was determined by the rod diameter at which the crack was appeared. Transparency of acrylate coated PET film was measured by UV-vis spectrometer (Lambada 9000, Perkin Elma). The transmittance at 550 nm was used as an optical transparency of PET film. To explore the characteristic of coated surface, contact angle was determined by contact angle measurement (Phoenix 300, SEO Co.) using distilled water.

Results and Discussion

Flexibility of Coated Films

Fig. 2 shows the flexibility of POS toughened acrylate coated PET film as a function of POS content. It was found that the flexibility increases with increasing POS content. Rollable diameter could be reached as low as 7 mm by adding POS up to 21 wt. % which satisfied the flexible substrate for electronics; indicating that the rubber toughening to acrylate took placed by adding POS. It seemed that the variation of chemical structures by modified POS did not give much influence on the flexibility of acrylate. Flexibly could be improved further by adding POS more than 21wt% but the oily surface was found in coated film surface due to the excess silicone in POS which is fatal defect for an optical film.

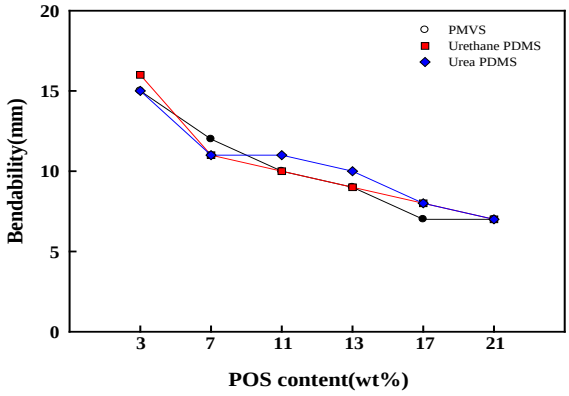

FIG. 2 FLEXIBILITY (BENDABILITY) OF POS TOUGHENED ACRYLATE AS A FUNCTION OF POS CONTENT.

Hardness of Coated Films

The effect of POS content on the hardness was presented in Fig. 3. The scratching depth was

improved over the amount of POS adding up to 21 wt. %. The lowering of scratching depth indicated that the acrylate coating layer became harder even though the rubber toughening was developed in acrylate. In general, if rubber is added to hard matrix, the matrix material should be softened by the rubber toughening but our results show that rubber toughening cause the increase of flexibility as well as maintain hardness like acrylate. This phenomenon was understood that POS acted as both a rubber toughening phase and crosslinking site with acrylate simultaneously. It was found that PMVS was more effective to the lowering of scratching depth compared to modified PDMS because PMVS consists of double bond in vinyl methyl group which is able to crosslink with acrylate.

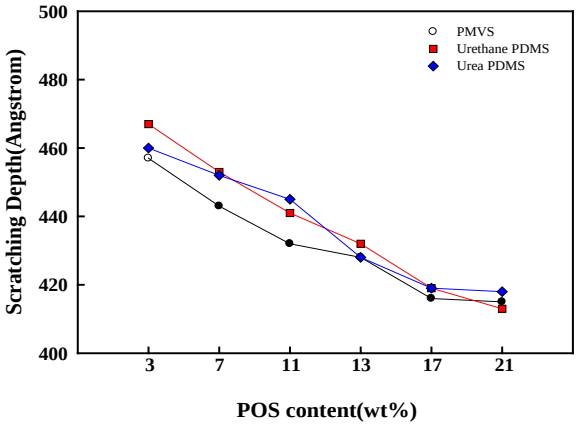

FIG. 3 THE HARDNESS OF POS TOUGHENED ACRYLATE COATED PET FILMS

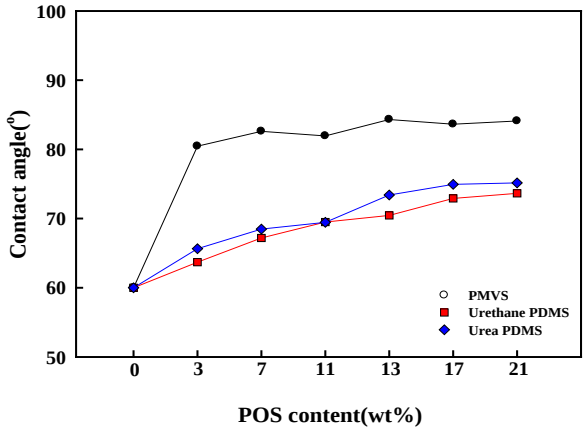

FIG. 4 CONTACT ANGLE OF POS TOUGHENED ACRYALTE COATED PET FILMS

Surface Properties of Coated Films

Fig. 5 shows the contact angle of POS toughened acrylate coated PET film. Acrylate coated PET film shows only 60° while the contact angle of POS toughened acrylate coated films increases up to 84° as increasing PMVS content in acrylate. It indicates that the surface of PMVS toughened acrylate coated PET film is changed to the hydrophilic surface due to the silicone molecule in PMVS. This surface characteristics might be either the advantage when this optical film is used for the anti finger printed film or the disadvantage for the printable film. In case of modified PDMSs toughened acrylate coated PET film, the hydrophilicity is much less compared to the PMVS toughened acrylate; implying that the chemical structure of POS is very important onto the surface characteristics of POS toughened acrylate.

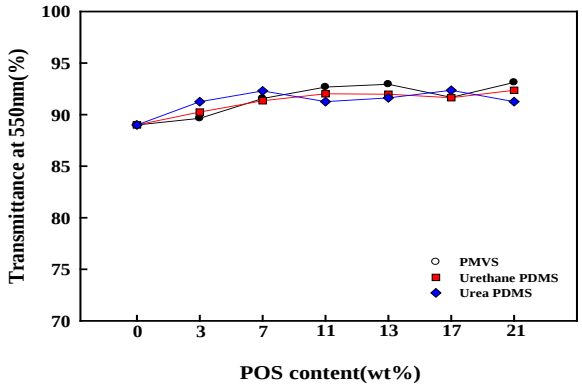

FIG. 5 OPTICAL TRANSMITTANCE OF POS TOUGHENED ACRYLATED COATED FILMS

Transmittance of Coated Films

Beside flexibility and hardness of POS toughened acrylate coated PET film, the optical transmittance is very important issue for protective optical film. Fig. 5 represents the optical transmittance of POS toughened acrylate coated PET films. It was found that even POS was mixed with acrylate up to 21 wt. %, there was no transmittance drop in POS toughened acrylate coated PET film compared to acrylate coated PET film; indicating that there was no phase separation between POS phase and acrylate phase since POS was well mixed with acrylate due to the compatibility of POS to acrylate and furthermore, it was crosslinked with acrylate by UV curing. Most of transmittance in POS toughened acrylate coated PET film was found to be over 90%, which was good enough to use this film as a flexible substrate. It was also noticed that there was no significant effect of chemical structure variation by modified PDMSs on transmittance.

Conclusions

POS toughened acrylate was studied to introduce the acrylate hard coating having flexibility and hardness in the same time. It was found that POS toughening in

acrylate resulted in the enhancement of both flexibility and hardness. It was explained that POS acted as rubber toughening phase as well as crosslinking site with acrylate. However, the surface characteristic of POS toughened acrylate became hydrophilic which reduced the printability of coated PET film. The surface characteristics might be controlled by applying modified PDMSs instead of PMVS. It was found that even though PDMS was added to acrylate, the optical transmittance could be maintained up to 90%, which was favourable for protective optical films.

ACKNOWLEDGMENT

This work was supported by the Advanced Technology Center(ATC) Technology Development Program of Ministry of Trade, Industry and Energy, Korea (No. 117773) and GRRC Program of Gyeonggi Province (GRRC Dankook 2011-B04, Development of advanced hard coating materials and processing methods).

REFERENCES

Holman, R. and Oldring, P., UV- and EB Curing Formulation of Printing Inks, Coatings, and Paints, Landon: SMA, 1991.

Kang, D. W., and Bak, S. W. "Ultraviolet-Curable Coating Material Composition and Hard Coating Film by Employing the Same." Korean Patent, No. 1020110096392, 2012.

Kang, D. W., and Bak, S. W. "Method for Preparing Polydialkylsiloxane Modified Urethane-Acrylate Compound, Polydialkylsiloxane Modified Urethane-Acrylate Compound Prepared thereby and Coating Composition Comprising the Same." Korean Patent, No.1020130056236, 2013.

Kim, Y. M. "Synthesis and Dielectric Properties of Polyimide Modified with Polyorganofluorosiloxane." PhD diss., Dankook University, 2001

Kuraoka, K., Ueda, T., Sato, M., Okamoto, T., and Yazawa, T. "Preparation and Properties of Organic-inorganic Hybrid Flexible Hardcoat Film." J. of Materials Science, no.40(2005): 3577-3579.

Ryntz, R.A., Abell, D. B., Pollano, G., Nguyen, L. H., and Shen, W. C. "Scratch Resistance Behavior of Model Coating Systems." J. of Coatings Technology, no.72(2000): 47-53.

Schwalm, R., Häußling, L., Reich, W., Beck, E., Enenkel, P., and Menzel, M. "Tuning the Mechanical Properties of UV Coatings Towards Hard and Flexible Systems.", Progress in Organic Coatings, no.32(1997): 191-196.

Takaki, S., Matsumoto, K., and Suzuki, K. "Properties of Highly Conducting ITO Films Prepared by Ion Plating." Applied Surface Science, no.33 (1988): 919-925.

Tanglumeler, W., Prasassarakich, P., Supaphol, P., and Wongkasemjit, S. "Hard-coating Materials for Poly (methyl methacrylate) from Glycidoxypropyltrimethoxysilane- Modified Silatrane via a Sol-gel Process." Surface and Coatings Technology, no.200 (2006): 2784-2840.

International Journal of Material Science (IJMSCI) Volume 4 Issue 1, March 2014 www.ij-ms.org
doi: 10.14355/ijmsci.2014.0401.07

Investigation on Relationship Between Energy Storage and Special Performance of L-arginine Phosphate Monohydrate (LAP) Crystal

Xitao Liu, Lei Wang, Luning Wang, Guanghui Zhang, Xinqiang Wang, Dong Xu*

State Key Laboratory of Crystal Materials and Institute of Crystal Materials, Shandong University
Jinan 250100, China, P.R. China

*xdoffice@sdu.edu.cn

Abstract

Phosphate arginine (PA) has been known as the medium carriers for bioenergy storage, while the similar structural substance L-arginine phosphate monohydrate (LAP) crystal is an excellent nonlinear optical crystal with a high laser-induced damage threshold. Energy storage in organism and laser-induced damage in crystals are both correlative to energy. Temperature dependence X-ray diffraction (XRD) and solid state NMR spectroscopy were performed to explore the impact of energy (heat and magnetic) fields on LAP crystal. XRD results reveal that LAP processes a reversible specific phase transition as the temperature changed. Saturation recovery experiments have shown that the crystal has a long proton spin-lattice relaxation time (^{1}H T_1) of 184 s with an amazing solid-state stability. The nuclear magnetic resonance (NMR) and fluorescence emission spectra of LAP solution compared with several amino salt solutions have also been investigated. The results show that the emission wavelength of LAP solution is blue-shifted from 415 to 380 nm. When energy (laser, heat, magnetic and etc.) fields are applied on LAP crystal, it processes a various of distinctive properties which make LAP a special material worthy of further detailed investigation.

Keywords

Energy Storage; Special Performance; LAP Crystal; Relationship; Biological Amino Acid

Introduction

The biological amino acid molecule is the basic unit to protein in organism, which participates in the function of the life. Phosphate arginine (PA) has been known as the medium carriers for bioenergy storage and transport by means of convertible transition between adenosine diphosphate (ADP) and adenosine triphosphate (ATP) in invertebrates, as phosphocreatine (PC) in vertebrates. As a basic amino acid, arginine is a linear chain molecule with a planar guanadyl group and an amino acid group at opposite ends. In many biological systems, the guanidyl group, which forms part of arginine side chain, plays an important role in the structure interaction and action of proteins. The functions of arginine are mainly related to its charge distribution and conformational variation through hydrogen bonds. In the biological process of energy transport, the conformation of arginine may change from a partly folded state to a fully extended state for external interactions.

L-arginine phosphate monohydrate (LAP) crystal which has the similar structural unit as PA was firstly discovered by Shandong University as an excellent nonlinear optical (NLO) crystal in 1983. Since then, LAP has been obtained a great deal of attention because of the outstanding properties such as high conversion coefficients (maximum to 90%) and extremely high laser-induced damage threshold (63 GW/cm^2 at 1053 nm and 1 ns). Its deuterated analog (DLAP) exhibits an even higher damage threshold. Recently, Japanese scientists have discovered and studied the stimulated Brillouin scattering (SBS) properties of LAP and DLAP crystals, and believed that their high laser damage thresholds are closely related to the SBS properties. However, it has not obtained a reasonable interpretation on the reason that LAP and DLAP possess such high laser-induced damage thresholds.

As we all known, energy storage in organism and laser-induced damage in crystals are both correlative to energy. The absorption spectrum study of LAP indicates the crystal has a relatively high absorption coefficient (especially in 1064 nm) corresponding to more energy absorption during laser radiation. Thus, the extremely high laser-induced damage threshold of LAP crystal should be some correlation with energy storage. In order to explore the relationship between them, a series of investigations were carried out in the present work. Temperature dependence X-ray

diffraction (XRD) and solid state NMR spectroscopy were performed to study the impact of energy (heat and magnetic) fields on LAP crystal. The nuclear magnetic resonance (NMR) and fluorescence emission spectra of LAP solutions compared with various of other amino salt solutions have also been investigated. The specific interactions involving the guanadyl groups and phosphate groups were also well discussed.

Experimental section

Temperature Dependence X-ray Diffraction

The XRD profiles of LAP simples as a function of temperature were obtained on a Rigaku D/Max-γA diffractometer, with Cu-target tube and a graphite monochrometer operating. The simples were placed perpendicular to the incident X-rays in an electrical hot stage in a nitrogen atmosphere. The sample was heated in stages from 20 to 90 using a heating rate of 5 °C min. The diffraction profiles were recorded at each selected temperature using a data accumulation time of 10 min. and kept at 90°C for two hours.

Solid State NMR Spectroscopy

Solid-state ^{13}C and ^{31}P NMR spectra were acquired using Chemagnetics CMX-300 spectrometers (Varian, Inc., Fort Collins, CO) operating at 500 MHz. The MAS frequency was 4.0 kHz, and the ^{1}H decoupling field was approximately 60 kHz. Recycle delays to acquire standard spectra varied based upon $^{1}HT_1$ measurements. Saturation recovery experiments were used to measure $^{1}HT_1$ relaxation times.

Nuclear Magnetic Resonance (NMR) and Fluorescence Emission Spectra of LAP in Solution

L-arginine (LA) and L-lysine (Lly) were provided from Sinopharm Chemical Reagent CO., Ltd. They were used without further purification. All the amino salts were synthesized in deionized water and purified by recrystallization process, respectively. The LA and LAP samples with D_2O as a solvent were prepared for ^{1}H-NMR, which concentration from 6×10^{-5} to 0.6 mol·L^{-1} and 5×10^{-5} to 0.5 mol·L^{-1}, respectively. The LA solutions of concentration from 6×10^{-5} to 0.6 mol·L^{-1} with deionized water as a solvent was prepared for fluorescence spectrum measurement. All ^{1}H-NMR spectra were recorded at 25 ºC using Bruker advance 300M spectrometer. Steady-state fluorescence spectrum measurements were performed using a Hitachi F-4500 fluorescence spectrophotometer and 1 cm quartz cell under physiological conditions. The fluorescence emission spectra were recorded from 300 to 600 nm using 10/10 nm slit widths at room temperature.

Results and Discussion

Temperature Dependence X-ray Diffraction

Fig 1. shows the powder XRD patterns of LAP over the temperature range of 20 to 90 °C. The XRD results reveal that several new diffraction peaks appeared as the temperature rises. The the intensity of the peaks increased when the temperature kept at 90°C for a period of time. Temperature decreased to a low temperature for a long time the peaks disappeared. The LAP crystal processes a reversible specific phase transition as the temperature changed. As a matter of fact, in the structure of LAP, the guanadyl group is strongly engaged with phosphate group through hydrogen bonds, and the specific interactions involving the two groups may be the important influence on the laser-induced damage and physical properties. When energy (laser, heat, magnetic and etc.) fields are applied on LAP crystal, it will process a various of distinctive properties.

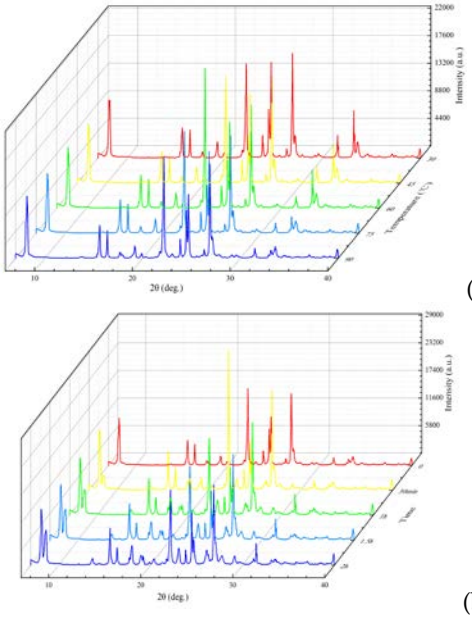

FIG. 1 CHANGE IN THE POWDER X-ray DIFFRACTION PROFILES OF LAP POWDER (a) AT TEMPERATURE RANGE FROM 30 TO 90 °C; (2) KEPT AT 90 OVER10 TO 2 HOURS.

Solid State NMR Spectroscopy

Saturation recovery experiments (Table 1) have shown that the crystal has a long proton spin-lattice relaxation time (^{1}H T_1) of 184 s, which is much larger than that of other crystals. The results indicate that LAP crystal has an amazing solid-state stability.

TABLE 1 PROTON SPIN-LATTICE RELAXATION TIME (^{1}H T_1) OF LAP COMPARED WITH OTHER CRYSTAL MATERIALS

	LAP	LABP	LA	LATF
^{1}H	184	≈2.5	2.55	≈2.5
^{13}C	500-1000	≈150	-	≈177.95

^{1}H-NMR Spectra

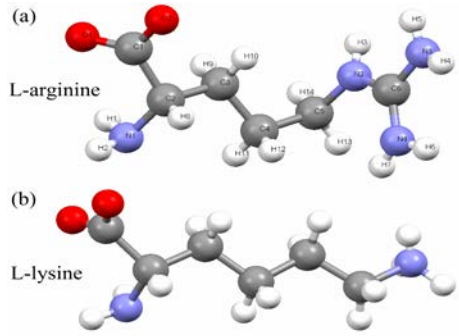

FIG. 2 MOLECULAR CONFIGURATION OF (a) L-ARGININE AND (b) L-LYSINE IN AQUEOUS SOLUTION

Since LA is dissolved in the solution in a zwitterionic form having a large dipole moment in aqueous solution, it tends to be aggregated to be nonpolar in a concentrated solution. The molecular configuration with atom numbering of LA in aqueous solution and is presented in Fig. 2(a). The greater acidity of proton and the greater sensitivity of its chemical shifts to the concentration of molecular, the chemical shifts of proton adjacent deprotonated carboxyl group (H8) were used to analysis molecular aggregation of LA and LAP in D_2O. The magnitude and nature of the shifts reflect differences in both the change of environment of the protons and their extent of involvement in the aggregation process. Molecular aggregation and the critical aggregation concentration (CAC) can be affirmed according to the following equation:

$$\delta_{obsd} = \delta_{mic} - CAC\frac{\delta_{mic} - \delta_{mon}}{C_t} \quad (1)$$

Where δ_{mon}, δ_{mic} and C_t are the chemical shifts of the monomer, aggregate and total solute concentration, respectively. The plot of δ_{obsd} versus $1/C_t$ for the LA and LAP solution are shown in Fig. 3. The plot of δ_{obsd} versus $1/C_t$ gives two straight lines with their intersection corresponding to C_t = CAC. On the basis of these plots, the CACs of LA and LAP solution have been derived, which are about 0.036 and 0.052 M, respectively. The tendency and CACs of molecular aggregation suggested the similar LA aggregate structure formed in LA and LAP solutions.

Fluorescence Spectra of LA and LAP Solutions

The steady-state fluorescence emission spectra of LA in different concentrations upon excitation at 340 nm are presented in Fig. 4. It can be noted that the fluorescence maximum of LA had two different emission bands (A and B in Fig. 4) at dilute and concentration solutions. The emission shifted from 430 to 415 nm at 0.05 M, which concentration is corresponds to CAC from ^{1}H-NMR. The fluorescence emission band of LA solution was centered at 415 nm, whose fluorescent chromophore should be LA aggregates.

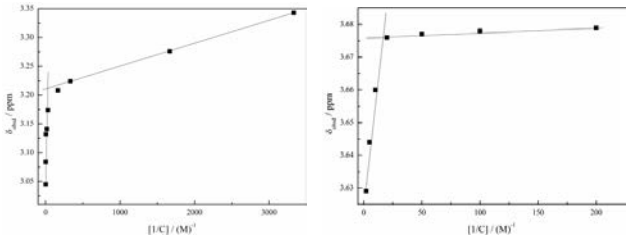

FIG. 3 VARIATION IN THE H8 CHEMICAL SHIFTS OF ARGININE MOLECULAR VS THE REVERSE OF CONCENTRATION OF (a) LA AND (b) LAP IN D_2O

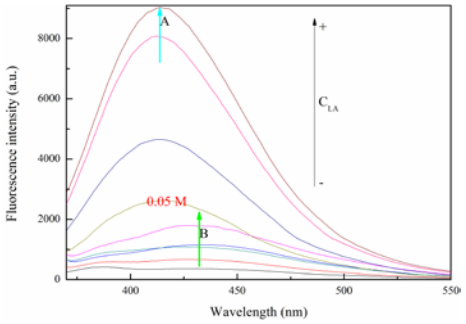

FIG. 4 FLUORESCENCE EMISSION SPECTRA OF LA IN DIFFERENT CONCENTRATIONS UPON EXCITATION AT 340 NM.

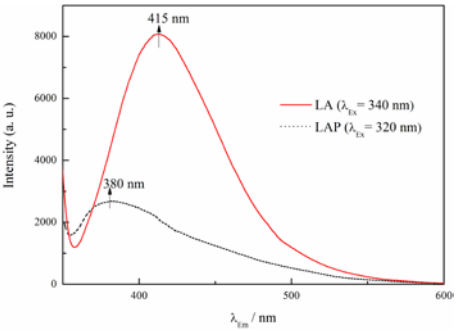

FIG. 5 EMISSION SPECTRA OF LA AND LAP AQUEOUS SOLUTIONS AT 0.5 M

The results of ^{1}H-NMR spectra have indicated the similar LA aggregate exist in LAP and LA solutions. Moreover, there is no other fluorescent chromophore in LAP solution. Fig. 5 gives significant differences in the measured emission spectra of LA and LAP aqueous solutions at 0.5 M. The excitation and emission wavelengths of LAP solution blue-shifted 20 (from 340 to 320 nm) and 35 nm (415 to 380nm) compared with LA, respectively. In LAP crystal

structure, no covalent bond and H-bond exist between LA and phosphate. Naturally no covalent bond formed between them in LAP aqueous solution for crystal growth. Thus, the blue-shifted of fluorescence spectra, indicated that the non-covalent interaction between phosphate and LA affected the structure of LA aggregate.

TABLE 2 FLUORESCENCE EXCITATION AND EMISSION BANDS OF SOME AMINO SALT SOLUTIONS

Amino salts	λ_{Ex} (nm)	λ_{Em} (nm)	pH value
LA	340	415	12.2
LAP	320	380	4.5
LATF	292	418	3.8
LAA	350	416	6.4
LANA	350	417	6.1
LATA	350	415	6.0
Lly	430	501	10.5
LLP	407	498	4.5
LLTF	408	496	3.8
LLTA	406	496	6.0
LLA	400	495	6.3

Fluorescence Spectra of Other LA and Lly Salts

In order to exclude the effect factor of ionic state on the fluorescence spectra, some kinds of other LA salts were synthesized and dissolved in deionized water. Their aqueous solution pH values are given in Table 2. The pH values of 3.8 to 6.4 can suggest that an ionic state same as in LAP solution exists more than 95% [22]. Thus, under our experimental conditions, LA ionic states and aggregates in these LA salt solutions can be analyzed as in LAP solution. While the fluorescent emission properties of LA salt solutions were similar as LA solution except LAP solution. The emission wavelength of LAP solution blue-shifted from 415 to 380 nm, suggesting the structure of fluorescent chromophore was affected by phosphate in LAP solution. Above all, the result indicated that the non-covalent interaction between LA and phosphate is distinct, and this interaction is independent of ionic state of LA molecular.

The L-lysine(Lly) molecular configuration is given in Fig. 2(b). It has a carboxyl group and an α-amino group which same as LA molecular, while the only difference between them is that the terminal amino group of Lly replaced the guanidine group of LA (Fig. 2b). Thus, there are no guanidine group in Lly and Lly salt solutions. The fluorescence excitation and emission bands of Lly and Lly salt solutions were given in Table 1. The excitation and emission wavelengths of Lly solution are 430 and 501 nm, respectively. Including LLP solution, the fluorescent emission properties of all Lly salt solutions were similar as Lly solution, whose emission wavelength at nearby 500 nm. Since the Lly fluorescent structure without guanidine group was not affected by phosphate, indicating that no special interaction existed between phosphate and the carboxyl or amino groups of Lly. Thus, in LAP solution, the guanidine and phosphate coexist affected strongly the fluorescent emission property of LA chromophore, indicating that the non-covalent interaction between guanidine and phosphate may be the reason of the LAP emission wavelength blue-shifted. The special non-covalent interaction between guanidine and phosphate affected the state of the molecular under the energy action in the solution.

Conclusions

Relationship between energy storage and special performance in L-arginine phosphate monohydrate (LAP) Crystal, have been explored. Temperature dependence X-ray diffraction (XRD) and solid state NMR spectroscopy were performed to study the impact of energy (heat and magnetic) fields on LAP crystal. XRD results reveal that LAP processes a reversible specific phase transition as the temperature changed. Several new diffraction peaks appeared when the temperature kept at 90°C for a period of time, while the peaks disappeared when the temperature decreased to a low temperature for a long time. Saturation recovery experiments have shown that the crystal has a long proton spin-lattice relaxation time ($^1HT_1$) of 184 s, which is much larger than that of other crystals. The results indicate that LAP crystal has an amazing solid-state stability. The nuclear magnetic resonance (NMR) and fluorescence emission spectra of LAP and various amino salt solutions have been investigated. The similar LA aggregate was discovered in LA and LAP solutions by ^{1}H-NMR spectra studies. LAP solution shown special fluorescence property compared with LA solution, which indicated the structure of LA aggregate chromophore was affected in LAP solution. Through the comparative study on the fluorescence property of other LA and Lly salt solutions, the factors of ionic state and the carboxyl or amino groups on fluorescence emission property have been excluded, respectively. Thus, the special interaction which affected chromophore fluorescence property could be confirmed to take place between guanidine and phosphate in LAP crystal growth solution. This non-covalent interaction may affect the state of the material under the energy action. Therefore, when energy (laser, heat, magnetic and etc.) fields are applied on LAP crystal, it will process a

various of distinctive properties, which make LAP a special material worthy of further detailed investigation.

ACKNOWLEDGMENT

The authors acknowledge the financial support of the National Natural Science Foundations of China (Grant Nos. 51102155 and 51372140), the Graduate Independent Innovation Foundation of Shandong University (Grant Nos. yzc12116), the Youth Scientist Fund of Shandong Province (BS2011CL025), the author of National Excellent Doctoral Dissertation (No. 200539) for China. the National Natural Science Foundations of Shandong Province (ZR2010EM039), and the Research Fund for the Doctoral Program of Higher Education (RFDP, 20110131120018). The Project also sponsored by SRF for ROCS, SEM.

REFERENCES

A. D. Headley, N.M. Jackson, J. Phys. Org. Chem. 15 (2002) 52.

A. S. Woods, S. Ferré, Amazing Stability of the Arginine−Phosphate Electrostatic Interaction, Journal of Proteome Research, 4 (2005) 1397.

A. S. Woods, S. Ferre, J. Proteome Res. 4 (2005) 1397

Auston,D.H. Ballman, A.A. et al. "Research on nonlinear optical materials: an assessment" Appl. Opt. 26 (1987): 211-211.

D. Xu, X.Q. Wang, W.T. Yu, S.X. Xu, G.H. Zhang, J. Cryst. Growth 253 (2003) 481.

E. Soderlind, P. Stilbs, Langmuir 9 (1993) 1678.

Eimerl, D. Velsko,S. Davis, L. Wang, F. Loiacono, G. and Kennedy, G. "Deuterated L-arginine phosphate: a new efficient nonlinear crystal. " IEEE J. Quantum Electron. 25 (1989): 179-193.

F. A. Cotton, V.W. Day, E.E. Hazen Jr., S. Larsen, S.T.K. Wong, J. Am. Chem. Soc. 96 (1974) 4471.

G.Dhanaraj, M.R. Srinivasan, H.L. Bhat, H.S. Jayanna, S.V. Subramanyam, J. Appl. Phys. 72 (1992) 3464.

H. Yoshida, M. Nakatsuka, H. Fujita, T. Sasaki, K. Yoshida, Appl. Opt. 36 (1997) 7783.

Liang Xian, Shuhua Liu, Yanqing Ma, Gongxuan Lu, Spectrochim. Acta A: Mol. Biomol. Spectrosc. 67 (2007) 368.

M.E. Morales, M.B. Santillan, E.A. Jauregui, G.M. Ciuffo, J. Mol. Struct. (Theochem.) 582 (2002) 119

M.Tang, A.J. Waring, R.I. Lehrer, M. Hong, Angew. Chem. Int. Ed. 47 (2008) 3202.

M.Yoshimura, Y. Mori, T. Sasaki, H. Yoshida, M. Nakatsuka, J. Opt. Soc. Am. B, 15 (1998) 446.

Meyerhof, O. "Über die Verbreitung der Argininphosphorsäure in der Muskulatur der Wirbellosen." Arch. Sci. boil. Napoli 12 (1928): 536..

N.Toyama, J. Kohno, F. Mafune, T. Kondow, Chem. Phys. Lett. 419 (2006) 369.

T.M. Clark, R.A. Lamb, D.F. Halsfead , CThH60.

Xu, D. Jiang, M.H. and Tan, Z.K. "A new phase matchable nonlinear optical crystal L-arginine phosphate monohydrate (LAP)." Acta Chim. Sinica 1(1983): 230-233.

Y.Zhao, S.J. Gao, J.J. Wang, J.M. Tang J. Phys. Chem. B, 112 (2008) 2033.

Yokotani, A. Sasaki, T. Yoshida, K. and Nakai, S. "Extremely high damage threshold of a new nonlinear crystal L-arginine phosphate and its deuterium compound." Appl. Phys. Lett. 55 (1989): 2692-2693.

Yoshida, H. and Nakatsuka, M. "Advanced Stimulated Brillouin Scattering for Phase Conjugate Mirror Using LAP, DLAP Crystals and Silica Glass." John Wiley & Sons, Inc. 2005.

Z.H. Sun, D. Xu, X.Q. Wang, G.H. Zhang, G. Yu, L.Y. Zhu, H.L. Fan, Mater. Res. Bull. 44 (2009) 925.